

72

Chambers

SPACE ENVIRONMENT SIMULATORS
FOR
SPACECRAFT TESTING AT GSFC

By
Henry Maurer, Jr.
Head, Thermodynamics Branch

November 17, 1964

FACILITY FORM 602

(ACCESSION NUMBER)	N 71-70442	(THRU)
(PAGES)	74	(CODE)
(NASA CR OR TMX OR AD NUMBER)	TMX-66519	(CATEGORY)

GODDARD SPACE FLIGHT CENTER
GREENBELT, MARYLAND

This paper has been prepared for presentation at the Symposium on Space Environment Simulators, sponsored by The British Interplanetary Society and The Society of Environmental Engineers, November 17, 1964, London, England.

SPACE ENVIRONMENT SIMULATORS
FOR
SPACECRAFT TESTING AT GSFC

By
Henry Maurer, Jr.

Introduction

Duplication of the space environment in a ground-based simulator is an ideal goal pursued by many, but accomplished by none.

Space environment simulators for spacecraft systems testing are rightfully born of trade-off's between knowledge of the environment and necessity for its simulation, weighed against cost and engineering ability to accomplish design and construction. The importance of simulating a single feature or several features of the space environment is dependent upon the space research task at hand, and varies accordingly with the trade-offs. Today's level of accomplishment in space simulation facilities for full spacecraft systems tests keynotes the early decision that proof of spacecraft performance under vacuum and thermal conditions representative of orbit is essential for success. Development and use of space thermal environment simulators at the Goddard Space Flight Center follows this trend. A general description of simulation facilities and test methods is covered by discussion of three simulators at the Center. It is noted that this survey omits a number of specialized simulators being used to calibrate various experiments, as well as those in use for specialized materials investigations. A brief

resumé of the Center's work furnishes orientation for the simulator discussion that follows:

The Goddard Space Flight Center was established in 1959 and is one of seven laboratories operating under the direction of the National Aeronautics and Space Administration. Within the NASA, Goddard is responsible for the development of unmanned satellites and experiments for exploration near earth and cislunar space. Three scientific areas are covered: communication, weather observation, and scientific technology. The space research program directed by Goddard is many faceted and dynamic. Magnetic fields, energetic particles, cosmic rays, atmospheric structures, aeronomy, solar physics, meteorology, ionosphere physics, geodesy, astronomy, communications, and spacecraft technology are but a few examples illustrating the vastness of its program. Goddard's space experiments fall into two categories: the sounding rocket space probe for brief sampling of the environment, and the orbiting spacecraft for prolonged measurements. Spacecraft are further categorized as Applications or Scientific. During the past five year period, Goddard has orbited over 30 such spacecraft. Figure 1 shows a number of those orbited and illustrates the variation in size and configuration. Familiar applications spacecraft include Echo, Relay, Syncom, Tiros and Nimbus. Most notable among the Scientific Spacecraft are the Explorers...Explorer X - P-14 Moon Magnetometer, XII - S-3 Energetic Particles, XVII - Atmospheric Structures, XVIII - Interplanetary Monitoring Probe, XX - Topside Scunder, Orbiting Solar Observatory, and the OGO I, Orbiting Geophysical Observatory. Goddard's active participation in international programs is highlighted by past accomplishments on Ariel I, Ariel 2 and Alouette.

In addition to its advanced spacecraft and experiment work, Goddard manages the development and launch of NASA's Delta rocket and launches Centaur and Atlas-Agena vehicles for the NASA program. In tracking and data reduction, the Center directs two worldwide networks: The Space Tracking and Data Acquisition Network (STADAN), and the Manned Space Flight Network (MSFN).

Test Philosophy

Within the Goddard organization, the Test and Evaluation Division is responsible for assessing the flight worthiness of spacecraft. Our test philosophy has been to concentrate on total systems testing. The integrated spacecraft undergoes environmentally-induced stress simulating ground handling, boost, and orbital environs for a sufficient time duration to reveal design and quality weaknesses. Due to time and economic reasons, systems tests are not directed toward establishing ultimate life or a statistical value for the reliability of the system. The philosophy is predicated on the concept that critical materials, parts, and subsystems have, in fact been tested. Prototype spacecraft are tested at elevated stress levels to qualify the design. In the design qualification tests, vibration amplitude is increased 50% and duration is twice that expected in flight. Predicted temperature extremes are extended 10°C to provide an overtest margin. Flight Spacecraft are tested at environmental stress levels which would not be exceeded during the launch phase of the mission more than once in 20 chances. Since duplication of the planned orbital life (one year) is not economically feasible, the duration of the orbital test is limited arbitrarily

to approximately 10 days. Failures attributed to subsystem interaction and "infant mortality" are detected and corrected. A graphical representation of this philosophy is shown in Figure 2.

Spacecraft Test Facility

During the 5 year period since its establishment, Goddard's spacecraft test facility has grown from a single vibration shaker, and a converted ocean buoy used for thermal vacuum tests to a highly sophisticated complex (Figure 3) housing over 46 pieces of environmental test equipment. (Figure 4) Development of this facility is based primarily on the concept of full spacecraft systems testing and has continued to grow with project needs from mechanically simple conditioning equipment to the highly complex space environment simulators. (Figure 5)

Space Simulator Development

Space environment simulator development for full spacecraft systems tests has progressed from facilities with vacuum and thermal capability to simulate the effect of the space thermal environment to chambers having light sources, cold shrouds and vacuum capability that more realistically simulate solar irradiation and the infinite heat sink of space.

Space Thermal Effects Simulation - Simulation of the effect of the space thermal environment has been applied extensively to evaluate spacecraft electrical and mechanical performance. Testing is accomplished by conditioning the spacecraft in a facility having the capability to produce vacuum of at least 10^{-5} torr under full spacecraft gas load, and thermal capacity sufficient to induce temperature conditions in the spacecraft equivalent to the extremes

predicted for orbit. During the test, stimuli are used to excite the experiment and spacecraft sensors whenever possible. Temperature extremes selected for test are based on the maximum and minimum orbital average temperature of the bulk spacecraft computed for a power off condition. With this method of testing, the spacecraft is normally operated during evacuation to reveal corona problems, then is stabilized under vacuum at each temperature level, and operated in its orbital mode. In cases where the predicted temperature of surface mounted equipment falls outside the range of the bulk spacecraft, separate thermal apparatus is required to provide a realistic test environment.

Facilities for this type of testing are similar to the unit shown in Figure 6. Typically, performance of this type of simulator is 10^{-6} torr, (CD&E)* and temperature from -65°C to $+100^{\circ}\text{C}$. The chamber in this example consists of a stainless steel enclosure forming an internal test volume 8' diameter by 8' long. The walls are highly polished to a #4 finish to minimize outgassing and trapping of contaminants. The pumping system (Figure 7) consists of a 30,000 liter/second oil diffusion pump backed by a 300 liter/second vapor booster pump, and 300 cfm mechanical pump. "Trapping" of the diffusion pump is provided by a concentric ring water baffle, and a chevron baffle operating near liquid nitrogen temperature. A radiation baffle plate is positioned inside the chamber in front of the throat of the pump to mask the spacecraft from seeing

* clean, dry and empty

the pump baffle. Thermal control for cold temperature conditioning is provided by either of two systems: CO₂ to Brine or Freon 22 & Freon 13 cascade to Brine. Hot conditioning is accomplished by a steam to brine heat exchanger. The transfer fluid is circulated through serpentine tubing placed in intimate contact with the outer chamber wall. Fiberglass insulation reduces thermal losses to a reasonable level. The space between the double "O" rings (Buna N) on the door, ports and penetrations is vacuum pumped to 50 microns Hg to increase the integrity of the seal. Total pressure measurement is done with alphasatron and ionization gauges.

During facility checkout and spacecraft tests, a mass spectrometer is mounted on the chamber to monitor outgassing constituents. Penetration plates for environmental and spacecraft performance data are shown at the side of the chamber (Figure 8). Figure 9 shows typical construction of connectors used for thermocouple, spacecraft data and high voltage power. The insulating material around each pin of the thermocouple and data connectors is Diaryl Phthalate, and for the high voltage connector, glass. The thermocouple connector has hollow pins for passage of the thermocouple wires through the connector for soldering external to the chamber. The "O" ring side of these connectors is compressed against the outboard face of the penetration plate as shown in Figure 10; leak rate is less than 1×10^{-8} atm. std cc/sec. Improved ground isolation for RF and high voltage applications has lead to the use of phenolic laminate (Nema grade XXX) penetration plates. Figure 11 shows "O" ring type connectors assembled to a typical phenolic penetration plate. For extreme high voltage

applications up to 30 KV, tapered pins are inserted through the phenolic and bonded with epoxy. For 30,000 volts, separation distance between pins of $2\frac{1}{2}$ " is typical. The vacuum and electrical performance history of these assemblies has been excellent.

The vacuum performance of this facility is shown in Figure 12 for ambient and cold conditions. These data are shown for a clean, dry, empty chamber and with a Delta size spacecraft installed. For this size spacecraft weighing up to 140 lbs., an outgassing rate of from 15 to 70 micron liters/sec. is typical. It is well to note that during test of a spacecraft, vacuum conditions are usually maintained throughout temperature transition periods. The test shown is an exception; the spacecraft was removed from the chamber and repaired prior to the hot exposure. When vacuum is maintained, time to establish stable temperature (-20°C to $+60^{\circ}\text{C}$) throughout a Delta class spacecraft (140 pounds typical weight) requires approximately 12 hours. Figure 13 shows a typical setup where separate conditioning was required to create a thermal gradient through the spacecraft. This method proves to be extremely time consuming when several temperatures in the spacecraft are being controlled simultaneously.

The adequacy of this type of facility for spacecraft tests performed in the manner described earlier is as good as one's ability to predict the orbital range of temperature at many sites throughout the spacecraft. The test provides an easy set-up for stressing the spacecraft under stabilized temperature and vacuum conditions, but is of only limited value in determining thermal paths through the spacecraft structure or between thermally-coupled subsystems. In brief, it does not provide an environment

necessary for checking the spacecraft thermal design, i.e. for validating the choice of extreme temperatures used for the test.

First Generation Solar Simulator

An interim space environment simulator having an internal, liquid nitrogen shroud, and carbon arc radiation source has been applied as a learning tool to bridge the gap between spacecraft thermal effects performance testing and thermal design testing.

In thermal design verification testing, the common link between the test environment and orbital temperature prediction is the thermal model. In this context, the thermal model is a mathematical simulation of the spacecraft. It consists of a series of equations describing the heat transfer at selected nodes throughout the spacecraft structure. The heat flow at a node is described by the following general equation:

$$\begin{array}{l}
 \text{(Heat Stored)} \quad \text{(Direct Sun)} \quad \text{(Albedo)} \quad \text{(Earth IR)} \quad \text{(Inter Power)} \\
 (mc)_i \frac{dT_i}{dt} = F_{Ai}' \alpha_i I_s + F_{Ai}' \alpha_i I_a + F_{Ai}' \epsilon_i I_e + P_{in} \\
 \text{(Rad. to Space)} \quad \text{(Conduct. between nodes)} \quad \text{(Radiation Between Nodes)} \\
 - A_i \sigma \epsilon_i T_i^4 - \sum_{j=1}^N K_{ij} (T_i - T_j) - \sum_{j=1}^N A_i \sigma F_{ij} (T_i^4 - T_j^4)
 \end{array}$$

$i, j =$ i th and j th nodes

$(mc)_i =$ Thermal Capacity

$T_i =$ Temperature, absolute

$t =$ time

$\alpha_i =$ Solar Absorptance

$F_{Ai}' =$ Area factor, including aspect angle of radiation

$A_i =$ Surface area

$I_s =$ Incident Solar Intensity

I_a	=	Incident Albedo Intensity
I_e	=	Incident Earth Radiation Intensity
P_{in}	=	Internal Power Dissipation
σ	=	Stefan Boltzmann Constant
ϵ_i	=	Infra-red Emittance
K	=	Thermal Conductance
F	=	Radiation Exchange Factor
N	=	Number of Nodes

The equation provides for stored heat, inputs due to solar, albedo, earth radiation and internal power, heat lost to space and conduction and radiation among nodes. In the mathematical handling for initial design, the major effort of the thermal designer is to supply numerical values for the coefficients. For a spacecraft system, the equation represents a system of N equations in N unknowns to the first and fourth power for which there is no direct analytic solution. Approximate solution is possible by iteration and matrix algebra. (Reference 3 discusses the process).

During thermal design verification testing of a spacecraft system, thermal capacities, conductances and radiation paths internal to the spacecraft are the same for the simulator test as in orbit. Since powered units can be operated in a sequence representative of orbit, the simulated radiation required to duplicate orbital temperatures at a node must meet the following:

$$F_{Ai} \alpha_{ei} I_{ci} - A_i \epsilon_{ei} \sigma T_{ci}^4 = F_{Ai}' \alpha_i I_s + F_{Ai}' \alpha_i I_a + F_{Ai}' \epsilon_i I_e - A_i \epsilon_i \sigma T_i^4$$

where $F_{Ai} \alpha_{ei}$ = Absorptance for incident radiation in the chamber

I_{ci} = Incident radiation intensity in the chamber

ϵ_{ei} = Total hemispherical emissivity of the spacecraft node in the chamber

Since the spacecraft coatings are duplicate of orbit $\epsilon_{ci} = \epsilon_i$ and the equation is reduced to the first term on the left equal to the first four terms on the right.

Advocates of the absorbed flux method of testing adhere to this concept. In practice, the α_{ci} of the spacecraft coating at the node is determined under the source illumination and intensity. I_{ci} is adjusted to a value where the product of I_{ci} and α_{ci} is equivalent to the sum of the input terms shown on the right hand side of the equation. Programming of source intensity permits an approach to dynamic simulation. This approach finds greatest application for spacecraft with simple geometry and those having a single thermal coating. Spacecraft with re-entrant shapes, multiple surface coatings and shadowing elements become extremely difficult to irradiate properly, and the method loses significance.

Borrowing from the absorbed flux concept, but concentrating on simulating solar irradiation which is usually the major thermal input to the spacecraft, an alternate approach can be most useful in checking the thermal design mathematical model. This concept consists of using a radiation source capable of closely matching spectral distribution of the sun in the wavelength band $.2\mu$ to 4.0μ and having controllable intensity, uniformity, and reasonable collimation. In this case, albedo and earth radiation are not simulated, and these terms are dropped from the thermal mathematical model. To provide useful thermal design data, the simulation must then meet the following:

$$F_{ai} \alpha_{ci} I_{ci} - A_i \epsilon_{ci} \sigma T_{ci}^4 = F_{ai}' \alpha_i I_s - A_i \epsilon_i \sigma T_i^4$$

Simulation of the solar aspect angle for proper area illumination and correcting for small errors in α_{ci} due to source spectrum and T_{ci}^4 , the shroud sink temperature, the test is simplified and yields useful data. In practice, the source and chamber are calibrated and temperature predictions are made for all nodes for the simulator environment. Variance between predicted node temperatures and those measured in-test provides insight into errors in the radiation or conduction coefficients used in predicting the node temperatures. The advantage of this method over absorbed flux simulation lies in the ability to properly illuminate complex shapes, evaluate geometric factors, and determine the actual absorbed flux typical of orbital direct sun insolation. While the above approach presents a means for handling variation between the simulator environment and space conditions, realistic performance testing of the spacecraft demands representative temperatures equivalent to orbit. In this sense, the more perfect the simulator for direct sun, albedo and earth IR inputs, the less difficult it becomes to accomplish both thermal design verification and the desired stress level required for the performance test phase.

Our first generation, small volume space simulator is shown in Figure 14. The chamber is a copy of the 8' X 8' facility, except the thermal control system has been omitted. A Cat-a-lac black coated, tube in sheet, aluminum shroud to provide a heat sink at near liquid nitrogen temperature (-196°C) is located internal to the chamber. A removable liquid nitrogen front panel provides access to the facility. Gaging and penetration plate capability is similar to the 8' X 8' system. A spacecraft

positioner capable of 2 axis motion; spin about the centerline of the spacecraft, and inclination relative to the incident simulated solar radiation, is located inside the liquid nitrogen shroud (Figure 15). During test, two modes of data transmission usually required are telemetry for spacecraft performance, and hardline for test temperature data and power control. The telemetry transmission is typical of orbital operation, while the hardline is handled through slip rings. The output of the numerous temperature sensors located on the test spacecraft are scanned by a compact multiplexer located inside the positioner pedestal and minimizes the number of wires penetrating the chamber. The thermal effect of attaching the spacecraft to the positioner is handled by an isolater-heater-sensor control mechanism. The mechanism senses the temperature at both the spacecraft side and positioner side of the interface and nulls out temperature differences within less than one degree. Radiation between the heater and spacecraft is masked by a shield operating at liquid nitrogen temperature. Under stable conditions, the mounting surface is considered to be a zero "Q" area, i. e. heat flow across the area is assumed equal to zero. This is represented in the math model used to predict in-test temperatures.

A twin 12kw carbon arc source is used to provide simulated solar radiation. The simulator is capable of an intensity of approximately 130 w/ft^2 over a 30" diameter target plane located six feet distance from the source. The beam enters the chamber through a one foot diameter quartz port and diverges approximately $7\frac{1}{2}^\circ$ -half angle. Each lamp is equipped with a 3 element reflector

to collect the arc radiation and project it forward to an optical flat for entry into the chamber. Figure 16 shows this set-up. Approximately $\frac{1}{2}$ of the target plane is irradiated by each lamp. Hand replacement of the rods requires approximately 1.5 minutes downtime for each arc per hour of operation.

Despite a forced air purge system, the systems reflectors (Figure 17) degrade in performance as they become coated with carbon deposit from the open arc. Reflector life is no better than 80 hours. The effect of the degradation during a test run is a decrease in total intensity and variation in local intensity. Maintenance of the desired average energy input to the test item is difficult and requires readjustment of the focus of the arc during the test. The uniformity of the output beam is poor. Intensity variation over a 23" diameter target plane measured with a rolled ribbon thermocouple detector ranges from $\pm 15\%$ to as much as $\pm 30\%$, depending on the condition of the reflectors. The poor uniformity, coupled with a depth of field change in intensity of 1% per inch of deviation fore or aft of the target plane (due to decollimation), places a severe burden on accurate pre-test calibration and intensity monitoring during the course of a test.

Calibration of the simulator for each test requires that the method used be capable of resolving the incident flux from the simulator source, and extraneous energy due to reflection or IR input from other apparatus in the chamber.

A calibration method used in the past incorporates an integrating black-ball device for measuring total energy and a rolled ribbon thermocouple radiometer for mapping the input intensity from the source. In addition, sample coupons, coated with the same thermal materials used on the test spacecraft, are pre-run in the simulator to determine absorptance coefficients and emissivity for the simulator environment.

The integrating black ball technique utilizes a thin shell aluminum sphere with a 1 inch diameter inner sphere suspended at its center. Thermocouples are attached to the inner sphere for temperature readout. Both spheres are coated with a black paint of known properties:

absorptivity (α) = 0.975 over the wavelength band 0.5 μ to 4.0 μ ; emissivity (ϵ) = 0.86 to 0.90 over the bandwidth 5 μ to 28 μ . During calibration, a sphere approximating the diameter of the spacecraft is positioned in the simulator at the exact location that the test spacecraft will occupy, the chamber is evacuated and the walls flooded with liquid nitrogen to simulate the same environment that the test spacecraft will experience. The sphere is rotated at a rate of 3 - 5 rpm to negate small errors in position of the inner sphere. The arc source is then adjusted to so that the ball system stabilizes at a pre-determined temperature. In this case, the ball sums the energy contributed directly by the arcs, plus any extraneous energy:

$$T_B^4 = \frac{Q_{in}}{\sigma A_T \epsilon_B} + T_S^4$$

- T_B = absolute temperature of the inner ball
- T_S = absolute temperature of the shroud
- σ = Stefan Boltzmann Constant
- A_T = total surface area of the outer sphere
- ϵ_B = emissivity of the outer sphere
- Q_{in} = total energy input

$$Q_{in} = A_p \alpha_B I_{ARC} + E_E$$

A_p = projected area of outer sphere

α_B = absorptance coefficient of outer sphere

I_{ARC} = average intensity from arc source over outer sphere (A_p)

E_E = Total extraneous energy

By assuming $E_E = 0$, the average arc intensity can be calculated:

$$I_{ARC} = \frac{A_r}{A_p} \frac{\epsilon_B}{\alpha_B} \sigma (T_B^4 - T_s^4)$$

Mapping of the beam is accomplished using a rolled ribbon thermocouple radiometer. The radiometer is calibrated using a National Bureau of Standards lamp of known spectral irradiance over the range of $.25 \mu$ to 2.6μ . Special computation extends this calibration range to 4.0μ . The radiometer temperature is held constant by a thermoelectric device and is used on an x-y plotter for measuring the incident flux from the source. Readings obtained across the target plane are area weighted and averaged. The resulting value is then compared with the I_{ARC} value previously obtained by calculation using the black ball. A difference greater than +5% is indicative of extraneous energy in the chamber. Experience has shown that removal or liquid nitrogen shielding of the extraneous energy sources is preferred over trying to account for them during the spacecraft test.

During the actual test of a spacecraft, continued monitoring of the arc beam is done with the radiometer to obtain local intensity data for input to the mathematical model. In addition, average intensity is determined as indicated above for readjusting the arc to maintain the desired input flux.

Inputs to the mathematical model to predict nodal temperatures for the spacecraft under test consists of local radiometer intensity values and the $\frac{\epsilon}{\epsilon}$ values from the coupons. It is well to mention that the intensity values obtained during test are input to the model with an allowance of $\pm 5\%$ for uncertainty. Manipulation of the model is done using these inputs. The resulting prediction thus establishes boundary limits for comparing node temperatures from the test. Nodes running outside the predicted temperature limits are investigated and corrected. Retesting is usually required where there is significant disagreement.

Experience with the arc source shows evidence of a fair match to solar irradiance in the wavelength band 0.2μ to 4.0μ . The absorptance coefficients of sample coatings of black and white paints and evaporated aluminum agree with computed solar absorptance values within 4% resulting in an $\frac{\epsilon}{\epsilon}$ difference of 9% for the worst case, evaporated aluminum.

The use of this first generation carbon arc source has served as an education in the problems of simulating solar irradiance. The variable uniformity of the system presents a most difficult problem and amplifies the uncertainties in the test. Despite the difficulty, test results show engineering significance and have lead to greater confidence in selecting maximum and minimum temperatures for the thermal vacuum performance test of several spacecraft.

Space Environment Simulator

The need for a large space simulator to test observatory class spacecraft weighing up to 4,000 pounds became

evident during early planning of GSFC's space research program. The obvious limitations in chamber size and small solar simulators for producing collimated and uniform radiation, precluded a simple scaling-up concept. Instead, a new approach beyond the state-of-art was needed to meet GSFC's minimum requirements. In 1960, the simulator specifications called for:

Working Volume:	27½' Diameter X 40' Height
Vacuum:	1X10 ⁻⁸ torr ultimate in 24 hours with full solar simulation
Thermal Shroud:	100°K and controllable between -65°C to +100°C
Solar Simulation:	
Area	20' Diameter
Intensity	50 to 275 watts/ft ²
Uniformity	±10%/ft ² throughout 17' diameter X 25' depth of irradiation
Collimation	4° -- ½ angle
Spectral Dist.	Equivalent to zero Air mass solar radiation from 0.3 to 4.0 microns

At acceptance in June of 1964, the simulator met the following:

Working Volume:	27½' diameter X 40' Height
Vacuum:	9.6 X 10 ⁻¹⁰ torr ultimate in 13 hours clean, dry & empty
Thermal Shroud:	105°K and controllable - 65°C to +85°C
Solar Simulation	
Area	20' Diameter
Intensity	50 to 130+ watts/ft ²
Uniformity	±10% per ft ² throughout 17' diameter X 25' depth

Collimation 2.2° -- ½ angle max.

Spectral Dist. Hg-Xe as modified by the optics

Two modes of operation of the simulator included:

1. Solar Simulation with the shroud maintained near LN² temperature (105°K)
2. Thermal Vacuum soak with the shroud held at a setpoint within the range of -65°C to +85°C.

The completed simulator is shown in Figures 18 and 19.

Major features include its vertical arrangement where the upper dome is removable for top loading of the test item. The upper dome houses the solar simulator and supports the solar plenum for cooling the Hg Xe solar lamps. An integral thermal shroud internal to the chamber covers the cylindrical section, upper dome and floor. A cryopumping shroud operating at 20°K extends for a height of 20' along the cylinder and is nested behind louvers on the thermal shroud. The two high arrangement of the oil diffusion pumps are backed by mechanical pumps at a lower elevation. The diffusion pumps enter the chamber through cylindrical members which are separated fore and aft of the thermal shroud to provide pumping of the inner chamber annulus and the test volume proper. The chamber is supported by a vertical skirt extending to the foundation. 12 column supports for the spacecraft table transmit the table load to the foundation.

The Vessel

The vessel structure is 33½' diameter by 60' high, fabricated from (ASTMA 240-58T) .75 inch thickness, type 304 stainless steel with external structure of (ASTM A7-59T) carbon steel. All vessel joints are through

welded for vacuum integrity, and internal surfaces are polished to a No. 4 finish to minimize outgassing.

The removable dome, having 127 - 6 inch penetrations for the solar system relay lens and supporting the solar lamp cooling plenum, is handled by an overhead mechanism which elevates the dome 12 inches, then laterally transports it a distance of 44 feet. The dome vacuum flange seal at the top of the chamber is shown in Figure 20. The dome load is supported by the chamber wall proper.

The 10' diameter stainless steel spacecraft support table at the 45 feet level can withstand loads up to 40,000 pounds. 48 vertical tee slotted, hardpoints arranged in tiers of 12 each are located at the floor, mid cylinder flange seal and dome. The hardpoints can support a load of 2,000 pounds each or a combined load of 40,000 pounds.

Although not man rated, the vessel is equipped with an 8 feet square air lock for personnel entry. Double doors 6½ feet square are sealed with double Buna N "O" rings.

Pumping Systems

The vapor and mechanical pump systems consist of 8 mechanical pumps and 8 blowers backing 17 - 50,000 liters per sec oil fractionating diffusion pumps. The system is arranged so that two mechanical booster pump groupings back 4 diffusion pumps (Figure 21). Rough vacuum is achieved with the mechanical boosters which pump the chamber through the diffusion pumps. After the required fore pressure is reached, the diffusion pumps are used to achieve ultimate vacuum. The diffusion pumps are connected to the chamber through liquid nitrogen cooled elbows, as shown in Figure 22.

Thermal Shroud

The thermal shroud consists of 0.156 inch thick aluminum panels with 1 inch tube passages. The arrangement forms nearly an optically dense enclosure inside the chamber. The shroud surface facing the test volume is coated with three coats of Cat-a-lac black paint with an absorption coefficient of approximately 0.96 and emissivity of 0.86 to 0.89 for the wavelength band 0.3μ to 24μ . The opposite surface is bright finished to reflect the heat radiated from the vessel wall. The thermal shroud operates below 110°K under pressurized single phase LN_2 flow, and between -65°C and $+85^{\circ}\text{C}$ with gaseous nitrogen as a transfer medium.

Table I shows a tabulation of significant features of the shroud assembly including vessel heat load and LN_2 demand. Additional LN_2 load due to cryo-elbows, and internal solar reflectors has been added for convenience.

TABLE I

SHROUD SECTION	NO. PANELS	TUBE SPACING	FLOW PATHS		VESSEL RADIANT HEAT LOAD	LN_2 FLOW FOR HEAT LOAD (qpm)
			LN_2	GN_2		
Top Dome	36	$15\frac{1}{4}"$	2	4	2.0 kw	1.5
Side Cylinder	36	$15\frac{1}{4}"$	6	12	9.6	50.0
Bottom	5	8	5	5	2.0 (117)*	87.6*
Pump elbows					7.1	3.6
Reflectors					1.8	21.9

* 275 w/ft² over 20' diameter area

The lower 20' of the thermal shroud supports the dense gas helium cryopumping panels shown in Figures 24, 25 and 26.

As mentioned before, the liquid nitrogen is designed to operate under pressure and single phase flow at all times. Load inequalities are balanced at a control panel shown in Figures 27 and 28. A 200 kw liquid nitrogen sub-cooler is used to provide capacity to remove absorbed heat from the circulating liquid nitrogen. Two 20 hp, 150 GPM, liquid nitrogen pumps provide circulation of the fluid through the shroud. A 5 hp, 10 GPM, liquid nitrogen pump is used for the cryo-elbows. A 1 kw (at 20°K) dense gas helium refrigerator provides the coolant for the gaseous helium shroud. 200 hp are required to obtain this amount of refrigeration. The cycle consists of compressing pre-cooled (23°K) helium gas and then passing it through an expansion engine (23°K --- 15°K). Figure 29 shows the control panel and cycle.

The warm gas system for obtaining temperatures between -65°C and +85°C consists of a gaseous nitrogen recirculation system wherein the medium is heated or cooled by three heat exchangers depending upon the temperature range of operation:

	<u>Shroud Temperature</u>
Steam to GN ₂	+85°C to +46°C
R-22 to GN ₂	+46°C to +65°C
LN ₂ to GN ₂	(supplements R-22 on Rapid Cool)

A 125 hp, 115 to 180 psia compressor is used for compression and circulation of the nitrogen gas through the shroud.

It is of interest to note that the vacuum system was sized on the basis of an assumed spacecraft outgassing load of 5×10^5 liters/sec at 1×10^{-6} torr. While no spacecraft have yet

been tested in this system, the best vacuum performance to date has been measured at 9.6×10^{-10} . Figure 30 shows a more typical pumpdown curve for the simulator. A simplified calculation of the pumping capacity of the system for its two modes of operation is shown in Table II.

TABLE II

PUMPING METHOD	SOLAR SIMULATION				THERMAL VACUUM SOAK			
	GAS PUMPED*				GAS PUMPED*			
	H ₂ O		N ₂		H ₂ O		N ₂	
	SPEED X10 ³ 1/sec	% TOTAL	SPEED X10 ³ 1/sec	% TOTAL	SPEED X10 ³ 1/sec	% TOTAL	SPEED X10 ³ 1/sec	% TOTAL
17 Diffusion Pumps	255	0.2	204	7	255	18	204	100
17 LN ₂ Elbows	1,139	1.7			1,139	82		
LN ₂ Heat Sink	61,000	92.9	2,720	93				
GHe Panels	3,380	5.2	2,720	93				
TOTAL	65,774		2,924		1,394		204	

* Assumed: Gas load = 95% H₂O, 5% N₂

Speed of diffusion pump constant from 10^{-3} to 10^{-8} and proportional to (molecular wt.)^{1/2} for gas being pumped.

Solar Simulator

The solar simulator system consists of 127 on-axis, Hg Xe powered modules spaced 20" apart to form a hexagonal array 20 feet in diameter (corner to corner). Figure 31 shows the array as viewed from the floor of the simulator. The array produces a 17' diameter beam of uniform irradiation

with decollimation no greater than $2.2^\circ - \frac{1}{2}$ angle. Intensity is adjustable over the range 65 w/ft^2 to $130+ \text{ w/ft}^2$. Uniformity of the beam is $\pm 10\%$ of the average intensity as measured by a 1 square foot detector throughout a volume of irradiation 17' diameter by 25 feet deep. Due to hexagonal arrangement, intensity drops to zero between the 17' and 20' diameter. The optical design of the array is such that each incremental area within the "volume of uniformity" receives irradiation from one to as many as seven modules, depending upon its location in the beam. For a point located on axis to a given module, and at a separation distance of 20', incident energy arises from the single module. For a separation distance of 45', the intensity at the point is the summation of energy contributed by 7 modules. Thus, the intensity distribution across a separate module as measured at 20' distance has a triangular shaped profile. Peak intensity occurs along the modules' optical axis, and falls off nearly linearly with distance from the center to the edge of the module beam. With this type design, the contribution of adjoining modules increases with separation distance and results in more uniform irradiation. Figure 32 illustrates this point. At the -10 ft. plane, significant shadowing by the hyperbola is evident. At the -20 ft. plane, the situation is reversed. Peak intensity occurs at the center of the module. At the -36 ft. plane, the amplitude of the oscillations have smoothed out and overall uniformity is improved.

Module Configuration

The heart of the system is the solar module. A schematic of the optical configuration is shown in

Figure 33. It consists of a 2.5 kw Hg Xe radiation source, elliptical collector, transfer optics and cassegrainian optics. The elliptical collector is front coated with aluminum and collects 85% of the lamp radiation. Transfer optics, consisting of 3 fused silica lenses, shape the energy for transfer by the fused silica relay lens. The emergent beam is then collimated by the cassegrainian optics located internal to the simulator environment. The relay lens forms the vacuum seal between chamber and upper optics. The cassegrainian system consists of a hyperboloid and parabolic reflector. The hexagonal paraboloid collimator measured 20" across flats and is electroformed nickel with the front surface coated with vacuum deposited aluminum. The hyperboloidal reflector is 4.10" diameter and is electroformed nickel bonded to a copper base. The front surface is vacuum deposited aluminum. Both reflectors internal to the chamber are cooled by circulating LN₂. The paraboloidal reflector is cooled by radiation. Air circulation of 100 ft³/min at 75°F is used to cool the upper optics. During operation, the hyperboloid and parabolic reflectors located in the chamber reach a temperature of 0°C and 23°C, respectively. Figure 34 is a photograph of the actual module elements.

The minimum efficiency of the module:

$$\frac{P_{\text{out}} \text{ (watts radiation)}}{P_{\text{in}} \text{ (elect power)}} \times 100 = 12.5\%$$

Average efficiency runs 13.5% with some modules showing a high of 14.5%.

Module alignment is done by pre-aligning the ellipse, lamp and cassegrainian assembly. The height of the transfer optics and the lamp ellipse combination with respect to the relay lens is pre-established by machine tolerance. Small lateral displacement in the upper optics is not particularly critical. The height of the lamp with respect to the ellipse is variable, however, and must be established for each unit to gain optimum uniformity. The height and centering of paraboloid-hyperboloid cassegrainian reflectors are also variable and must be pre-aligned before assembly. In practice, the lamp is centered in its holder and set to fixed height with respect to the holder reference surface. Each ellipse is mounted in a "standard off-line module" and it's reference surface is adjusted by shims to a preferred height where a pre-aligned lamp will yield maximum collection. Any anomaly in ellipse contour is adjusted for by the shims. The cassegrainian unit is assembled, centered and placed in the "standard module" for a final check for skewness. Once aligned, the subassemblies are interchangeable with other module units. During operation, burnt lamps may be replaced with a pre-aligned unit without further alignment. In the system installation, GN_2 is distributed over each relay lens and first meniscus lens. Positive flow assures that condensation will not occur at the relay lens during periods when the chamber is operating cold (but solar is not being used). In addition, any dirt that may become dislodged in the plenum, or from above when the lamp starter is removed, is blown clear of the meniscus lens.

Power and Control

Each module is powered by a 5.0 kw DC saturable core (Silicon) rectifier power supply. The supply is capable of adjustable current from 20 to 100 amperes and at full load, 50 ± 5 volts. Nominal lamp operation at 2500 watts is 50 amps @ 50 volts. A starter for each lamp provides 40 to 60 KV peak to peak at 1 to 3 mc for 3 seconds maximum to establish arc operation. Lamp stability is established in approximately 6 to 10 minutes.

Intensity control is obtained by servo loop circuitry, and a cadmium sulfide detector located in the upper plenum on each ellipse. A portion of the energy spilled by the ellipse is reflected to the detector aperture such that a change in intensity is sensed as a resistance change in the detector. Under automatic control, the detector signal is amplified and transmitted to a null detector, which is also supplied with a common reference signal, generated in proportion to the desired radiation intensity called for at the test floor. Lack of null produces a raise or lower signal to the individual lamp power supply. Power is automatically adjusted until null occurs.

Spectral Energy Distribution

The simulator is equipped with fixed instrumentation to monitor the spectral distribution of the output beam. Figure 35 shows the optical boom located at the 25' level, for intercepting the beam and relaying it to a modified P.E. 112U monochrometer. The diffuse reflector at the end of the boom directs the energy to optical flats arranged at the pivot axis. One flat is held fixed, while the other rotates with the boom. The collected beam exits the chamber through a quartz port where it is analyzed by the

monochrometer. The intensity vs. wavelength data is handled automatically by a central data collection system servicing the facility. The possibility of the mirror surfaces becoming contaminated in the chamber has been considered, and work is currently being done to provide a protected calibration source inside the chamber.

Spectral data available on the module has been obtained in a series of off-line experiments. The spectral energy distribution of the bare Hg Xe lamp is shown in Figure 36. In the module application, however, this spectrum is modified by the optical train. Table III presents a comparison of the spectral energy distribution of a module and carbon arc system (3 refracting quartz elements) vs. the energy distribution of sun at air mass zero. All values are normalized so that the bandwidth 1500 Å to 40,000 Å contains 100% of the energy.

TABLE III

	% ENERGY PER WAVELENGTH RANGE (Å)		
	U.V. 1500-3442	VISIBLE 3442-7168	IR 7168-40,000
Solar (a)	4.21	46.59	49.20
Module (b)	7.85	48.87	43.28
Carbon Arc (c)	3.66	38.97	57.37

- (a) From Johnson, Spectral distribution at air mass 0
- (b) From measurement using Eppley Lab. narrow bandpass filters, 12-C6
- (c) P.E. monochrometer, Model 112u, 1P28, PbS & Thermocouple detectors

Comparison of the absorption coefficient of several commonly used thermal coatings is shown in Table IV.

TABLE IV

COATING	SOLAR α^a	C.A. α^b	ΔT^c , °K	Hg-Xe MODULE α^d	ΔT^c , °K
Evaporated Aluminum	.078	.075	- 4.7	.071	-11.7
Leaf Aluminum Paint	.279	.277	- 0.7	.276	- 1.0
Evaporated Gold	.192	.162	-27.3	.237	+35.0
White Paint ZnO/K ₂ SiO ₃	.269	.260	- 1.4	.373	+22.0
White Paint Ti O ₂ /K ₂ Si O ₃	.204	.209	+ 1.4	.336	+30.9

- (a) From Johnson spectral distribution @ air mass zero
- (b) Spectral distribution of Strong Arcromatic, National Orotip cored rods, using P.E. 112U, 1P28, PbS & TC detectors
- (c) Cal. Temp. difference for flat plate, radiation at normal incidence, both sides coated, in space
- (d) From spectral distribution of single module at 1" off optical axis, 20' distance from optics with Eppley Lab. C-6 filters. Hg-Xe at 2.5 kw input power

Operation of the entire simulator is monitored at a master control console, shown in Figure 37. A graphic mimic panel displays the operational status of all systems.

Figure 38. Remote control of the LN₂, GN₂, GHe, Solar and Vacuum systems is enabled at the console. Automatic vacuum start, vacuum emergency stop, and setting of the solar intensity level is controlled only at the console. A

communication link for 12 remote stations is shown at the left of the console. Closed circuit television coverage of events in the simulator is provided by any of six cameras viewing the test volume. Picture selection is possible at either the console or mimic panel.

Preparations are currently underway to complete detailed calibration of the simulator. Figure 39 shows an R-Ø-Z scanning mechanism being used to map beam intensity throughout the test volume. At completion, an extended test of 60 days duration will be performed on the back-up model of Ariel 2 to establish failure mode in the spacecraft under long term temperature and vacuum exposure, and to gain confidence in the operation of the simulator for long term tests. The spacecraft positioner to be used for this test is shown in Figure 40. The long term exposure of a spacecraft under simulated test conditions is unique, and hopefully, new insight will be gained from the test.

This survey has pointed out only a few of the most obvious features of space environment simulators being applied by GSFC for full systems tests. Simulation of the space thermal environment is being approached, however, it is not being duplicated. Improved radiation standards, testing technique, and radiation monitoring in the simulator environment are required to limit the uncertainties in tests currently being run. The learning process required to relate space simulator tests to orbit conditions is challenging and, just beginning.

REFERENCES

1. J. C. New - "Experiences in Simulating the Space Environment for Scientific Satellites" , First International Congress on Vacuum Techniques in Space Research, 1964, Paris, France
2. J. C. New - "The 20 Foot Solar Simulator at the Goddard Space Flight Center", Proceedings, Fifth Annual Symposium on Space Environment Simulation, AEDC, 1964
3. M. Schach and R. E. Kidwell, Jr., "Thermodynamics of Space Flight (Heat Transfer Phenomena in Space)" GSFC Report X-633-63-50, 1963
4. Dr. M. P. Thekaekara - "Spectral Energy Distribution of a Mercury-Xenon Lamp", Section 2 of "Final Report of the Goddard Summer Workshop Program", X-320-62-193
5. R. W. Sheffield, "The Vacuum and Cryogenic Systems of Large Space Simulators", Proceedings, IES, 1963
6. R. E. Bernier, R. H. Hoffman, A. R. Timmins, E. I. Powers - "Solar Simulation Testing of an Earth Satellite at Goddard Space Flight Center", Proceedings, IES, 1964
7. F. Brown, "Spacecraft Outgassing Under Vacuum", Internal ART Program Progress Report, GSFC, 1963
8. G. M. Biddison, "Special Purpose Feed-through Plates for Thermal-Vacuum Chambers", Internal Memorandum, GSFC, 1963

ACKNOWLEDGEMENTS

The information presented in this paper represents the contributions of staff members of the Thermodynamics Branch, Test and Evaluation Division, Goddard Space Flight Center. The author would particularly like to acknowledge the contributions and assistance of Messrs. Raymond Kruger, R. T. Hollingsworth, M. Thekaekara, N. Zylich and A. Retzler. My thanks to Mrs. E. Ford, Messrs. R. LeDoux and E. Lechtenstein for manuscript and art work.

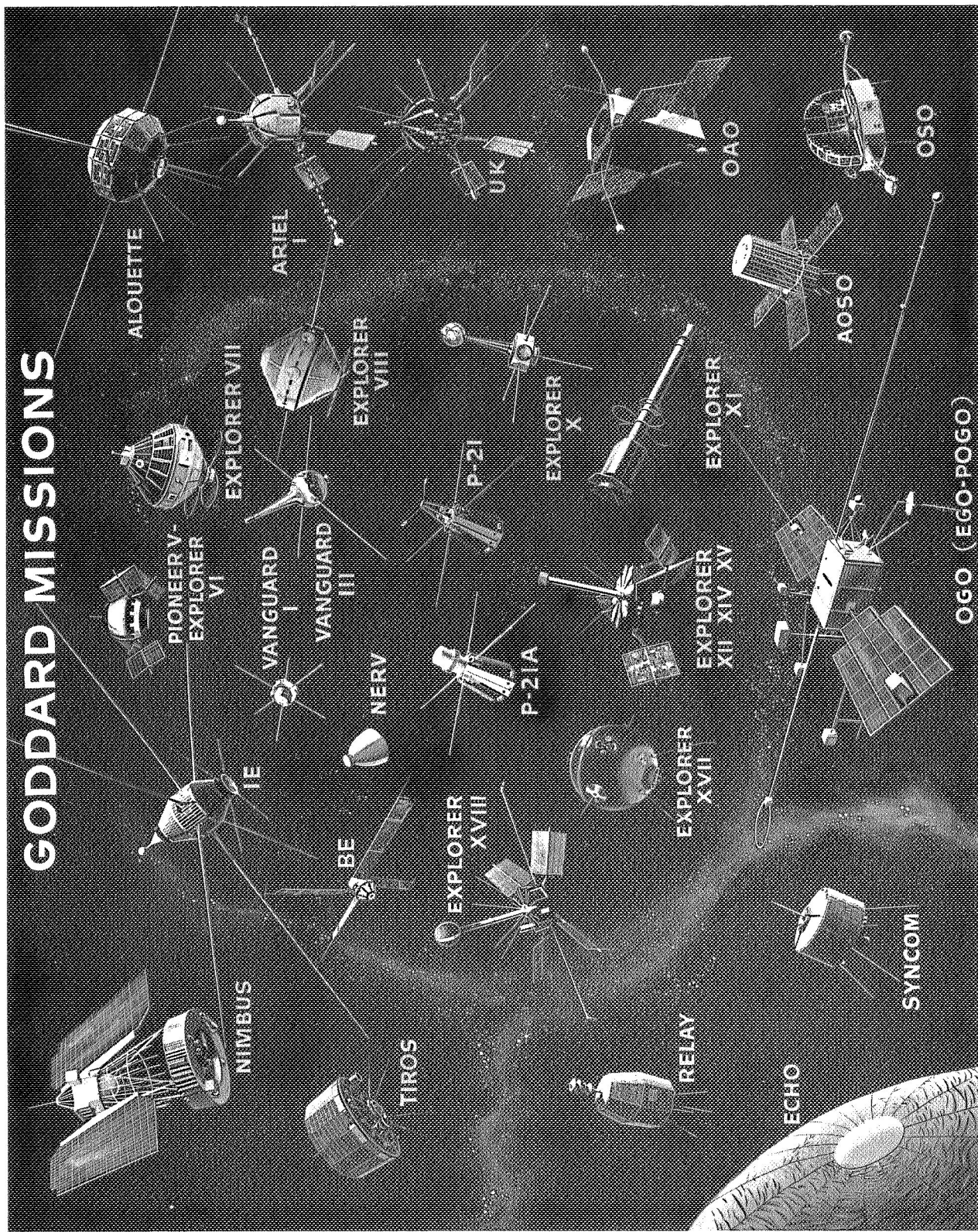


Figure 1. Goddard Missions

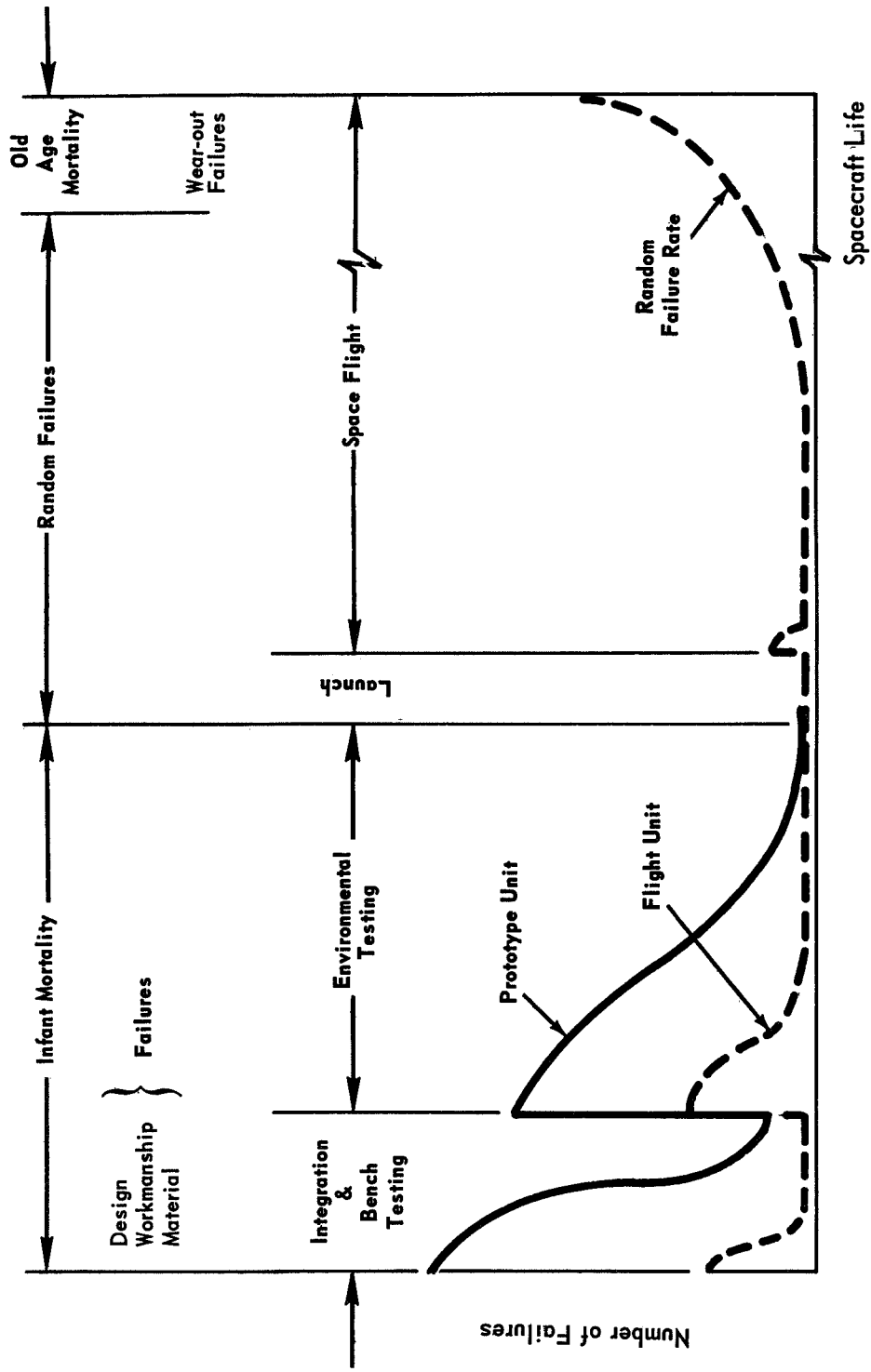


Figure 2. Failure Pattern

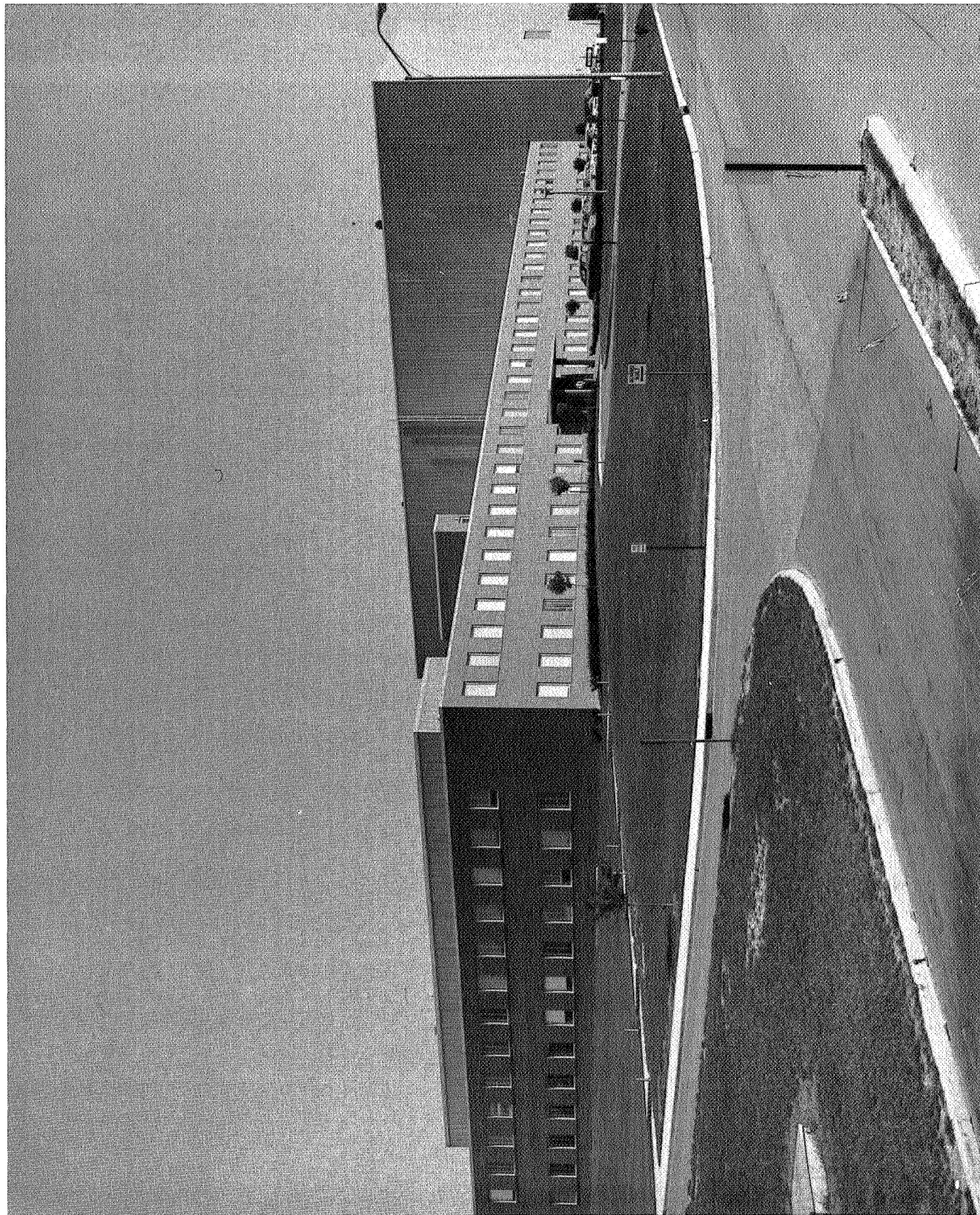


Figure 3. Spacecraft Test Facility

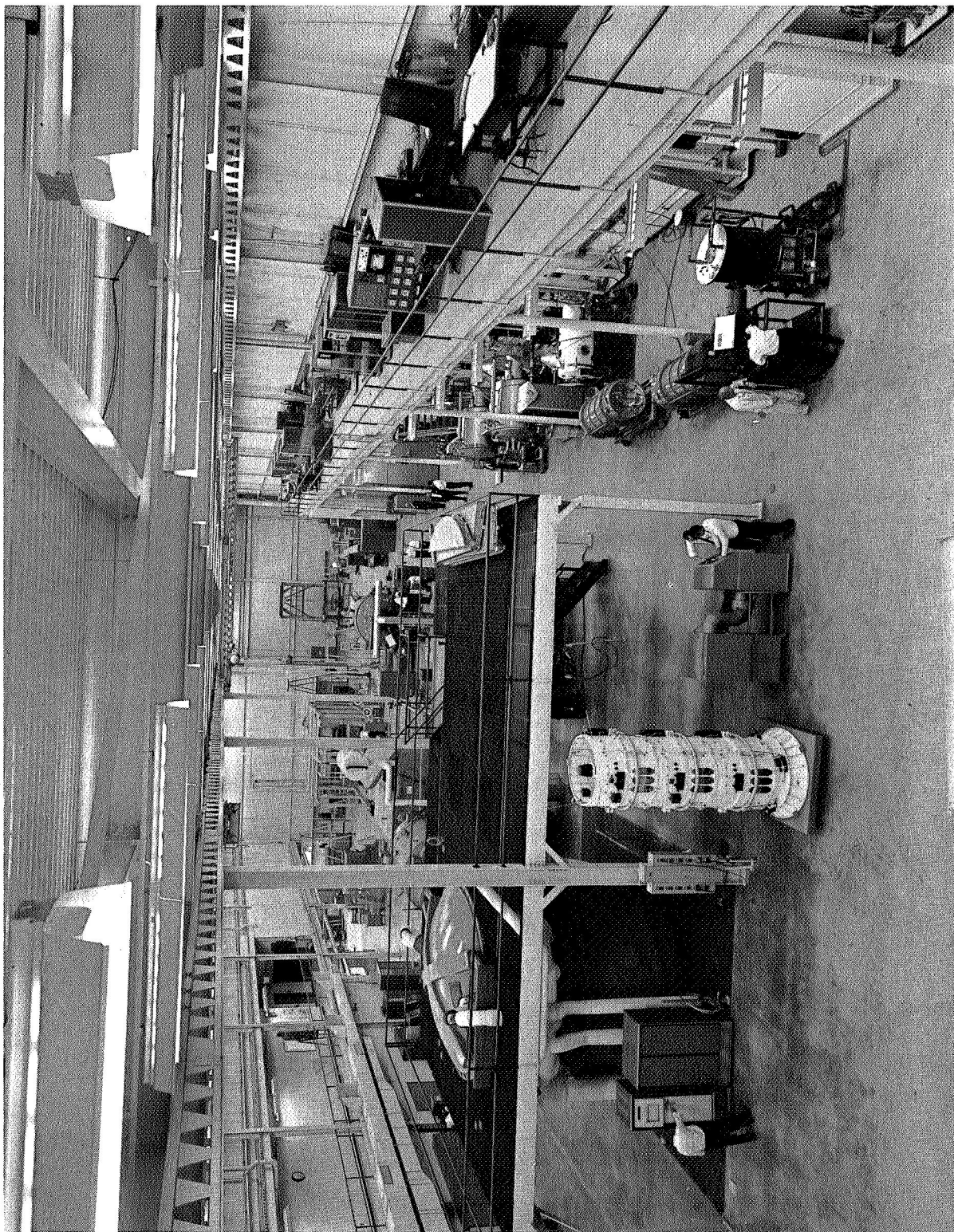


Figure 4. Building 7 Laboratory

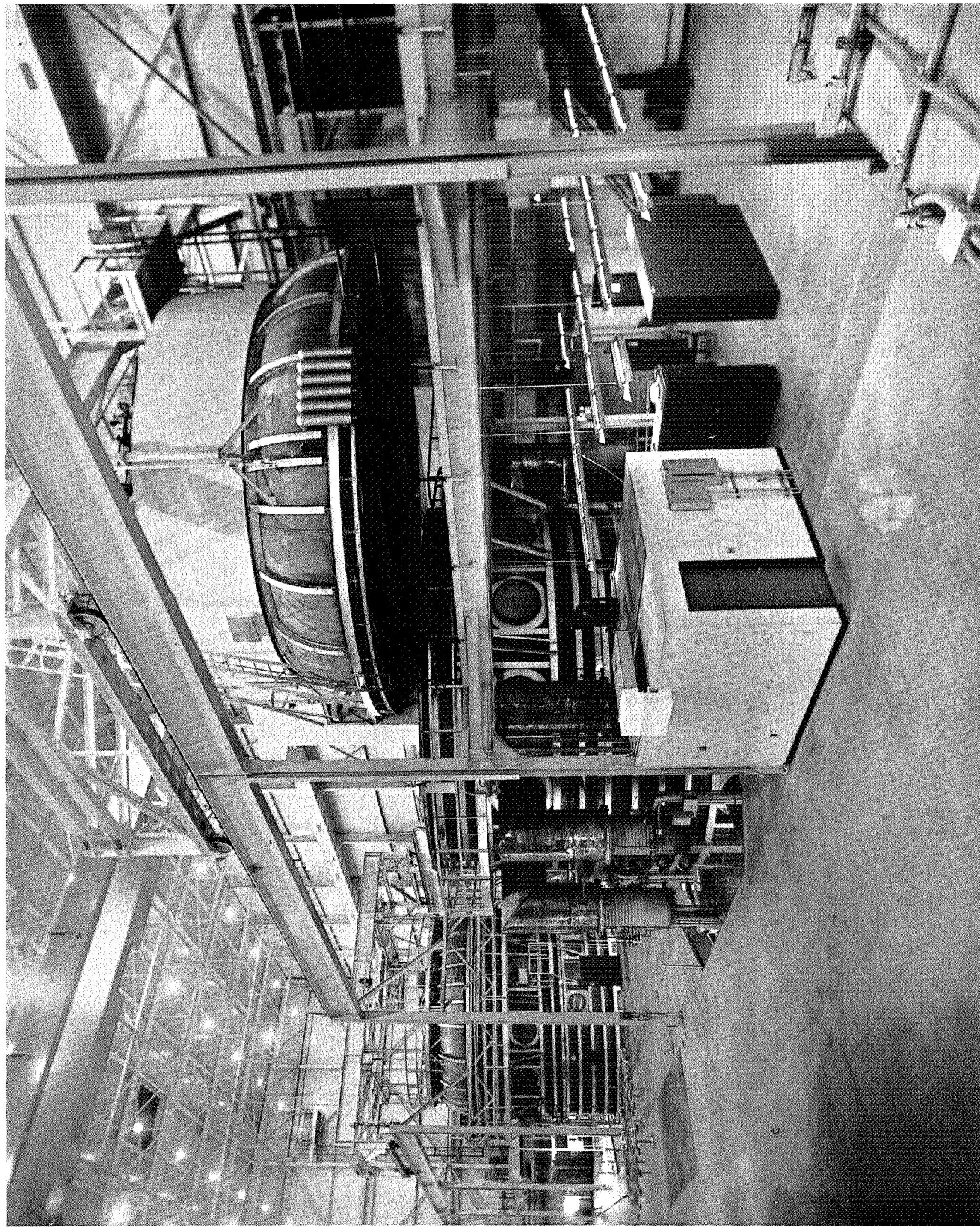


Figure 5. Building 10 Laboratory

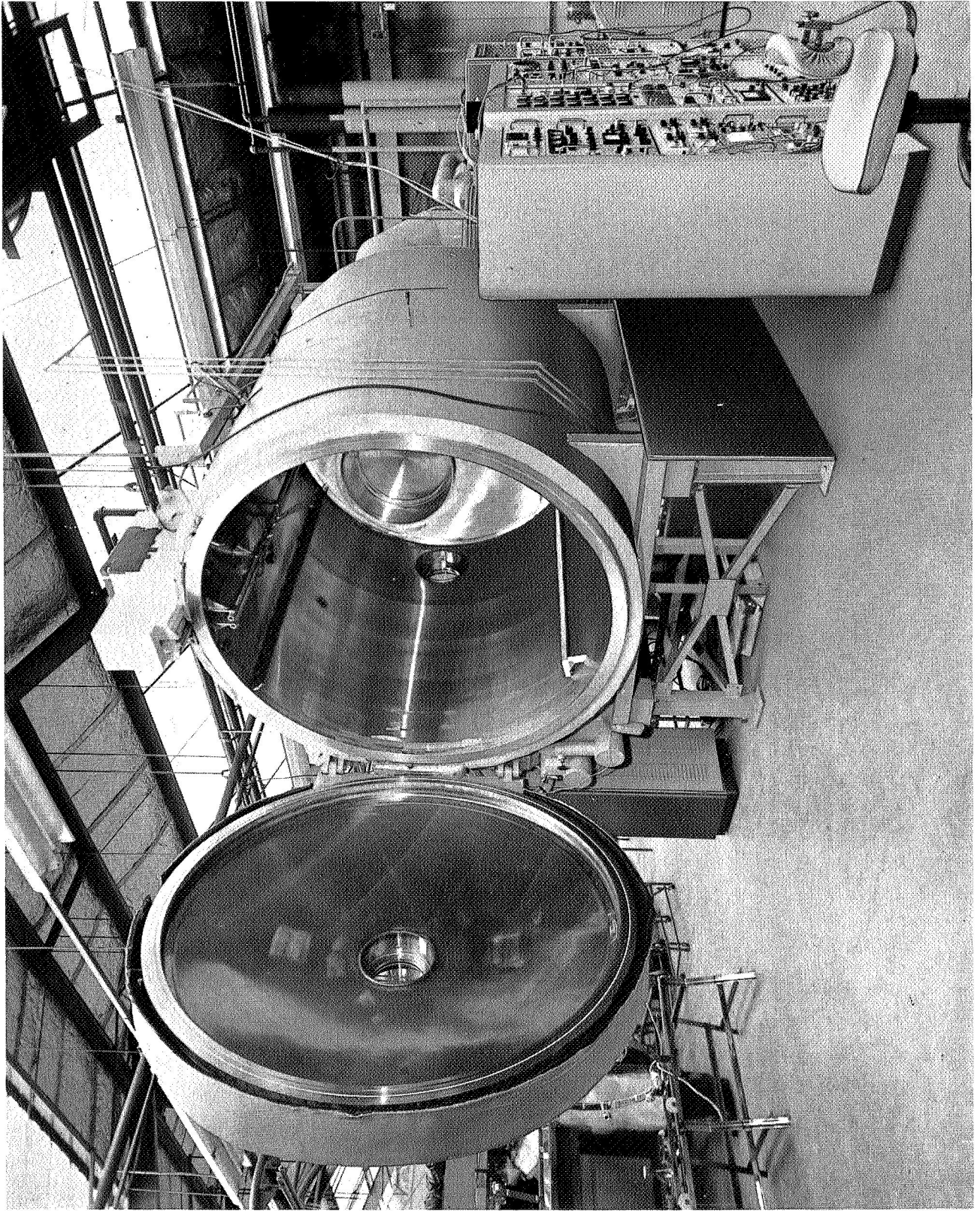


Figure 6. 8 X 8 Thermal-Vacuum Facility

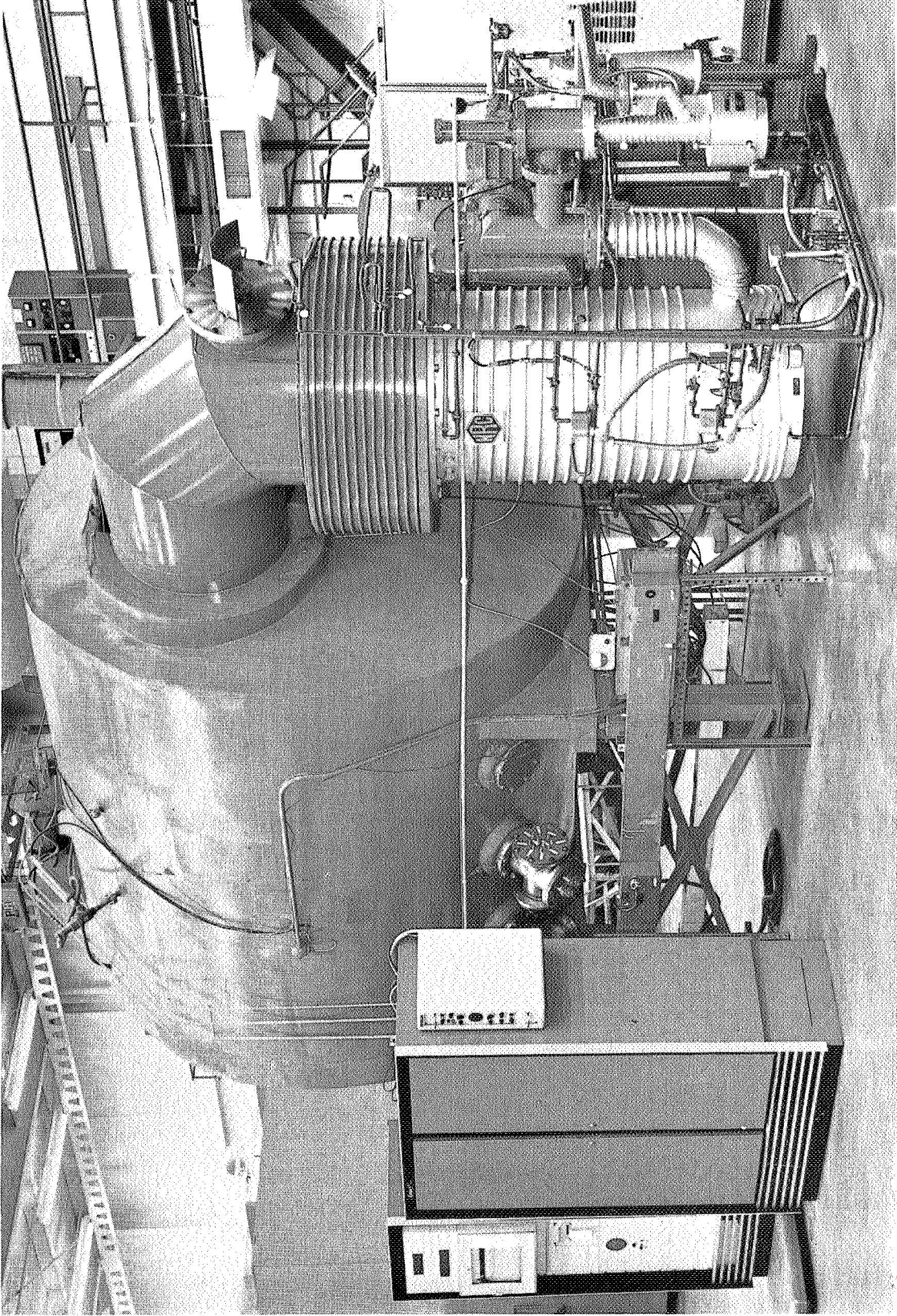


Figure 7. 8 X 8 Thermal-Vacuum Facility

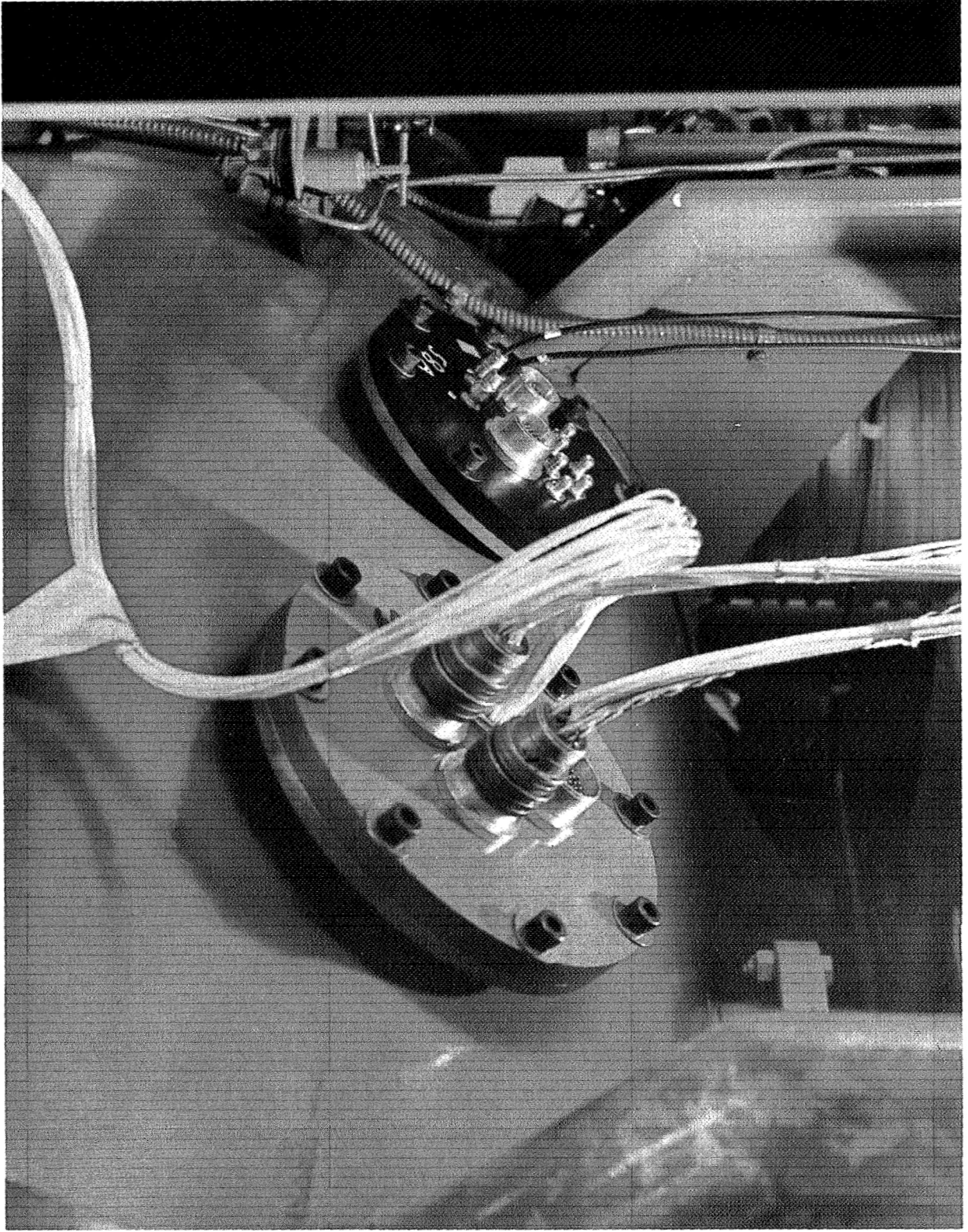


Figure 8. Penetration Plates on Facility

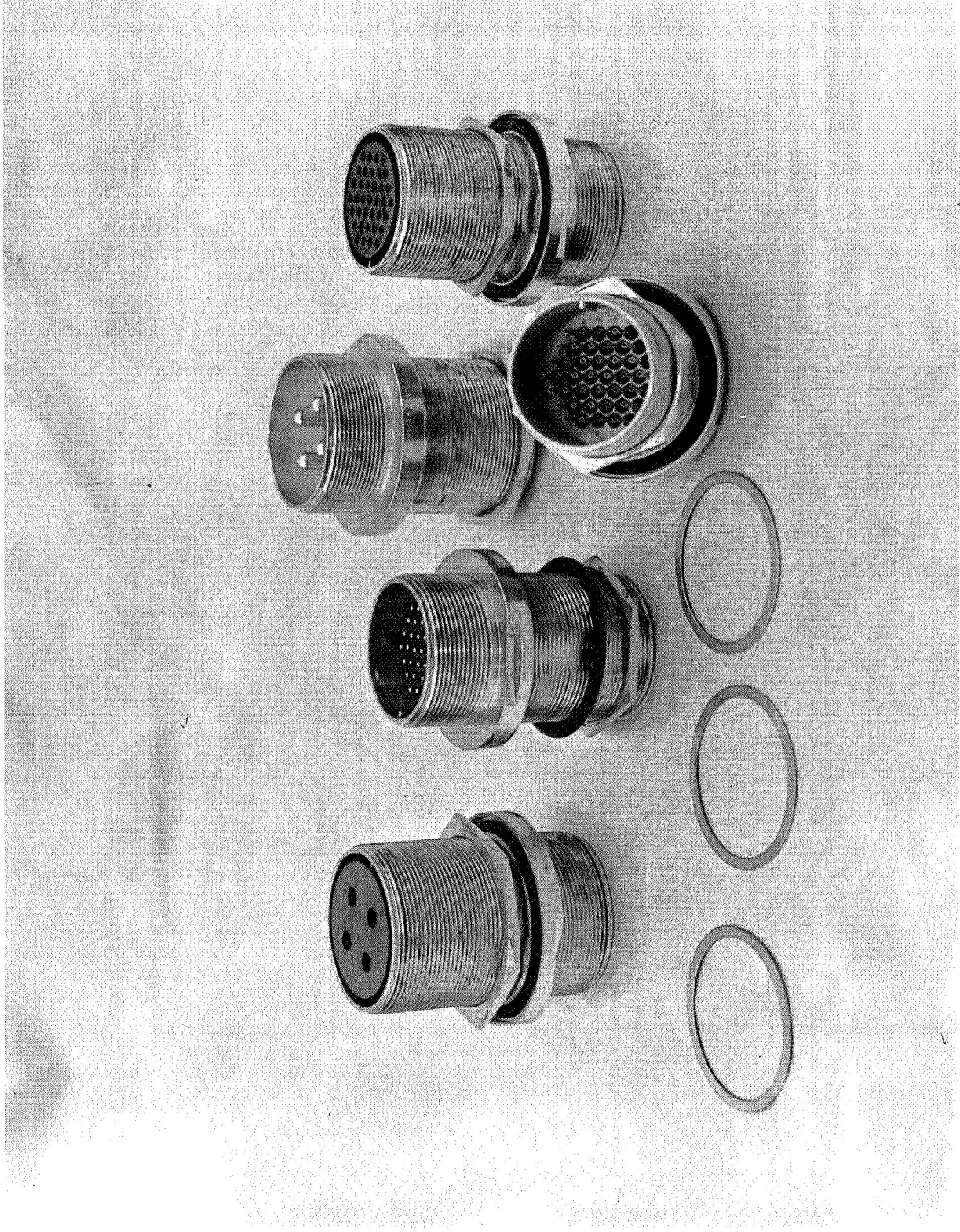


Figure 9. Feedthrough Connectors High Voltage Data Thermocouple

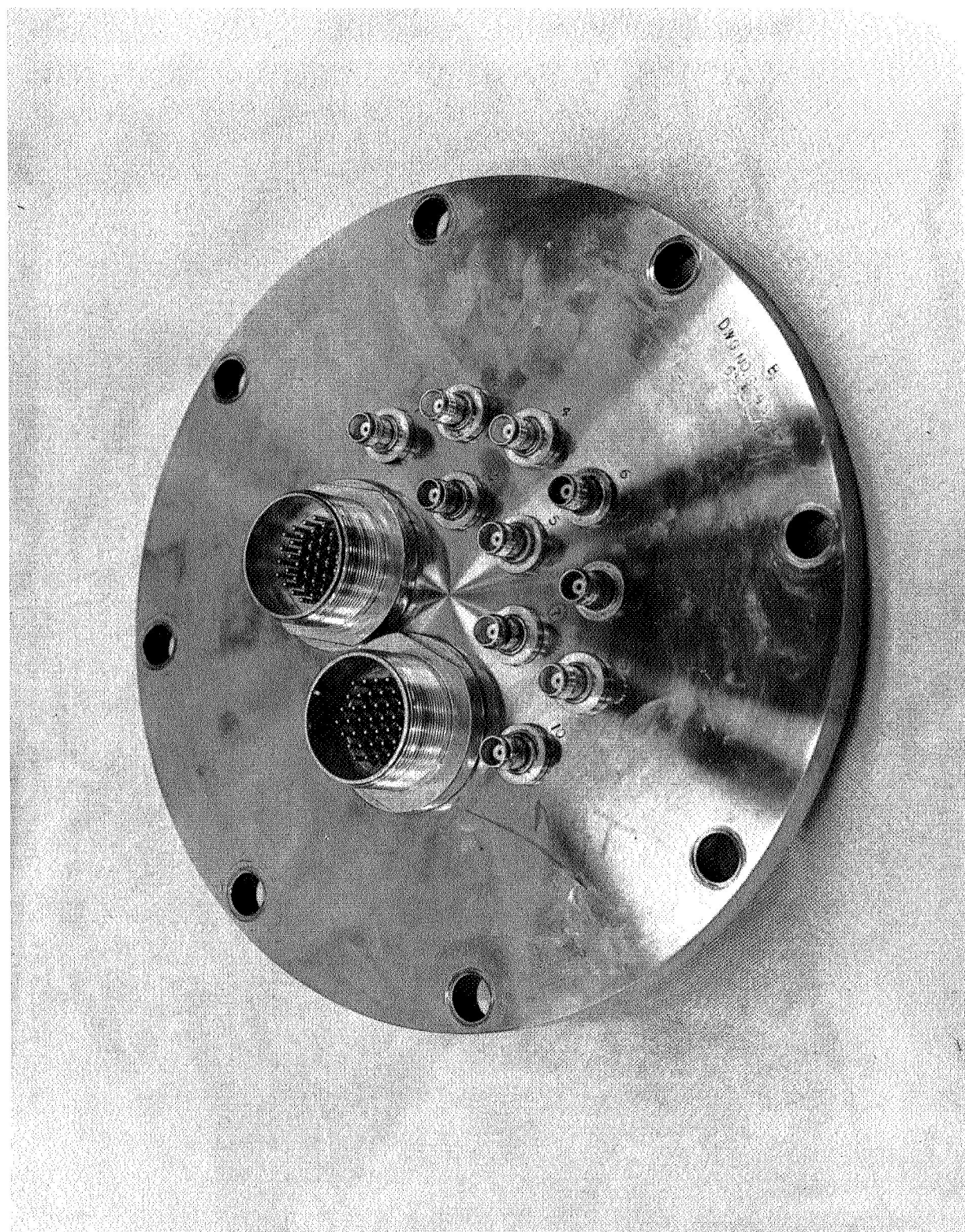


Figure 10. Stainless Steel Penetration Plate

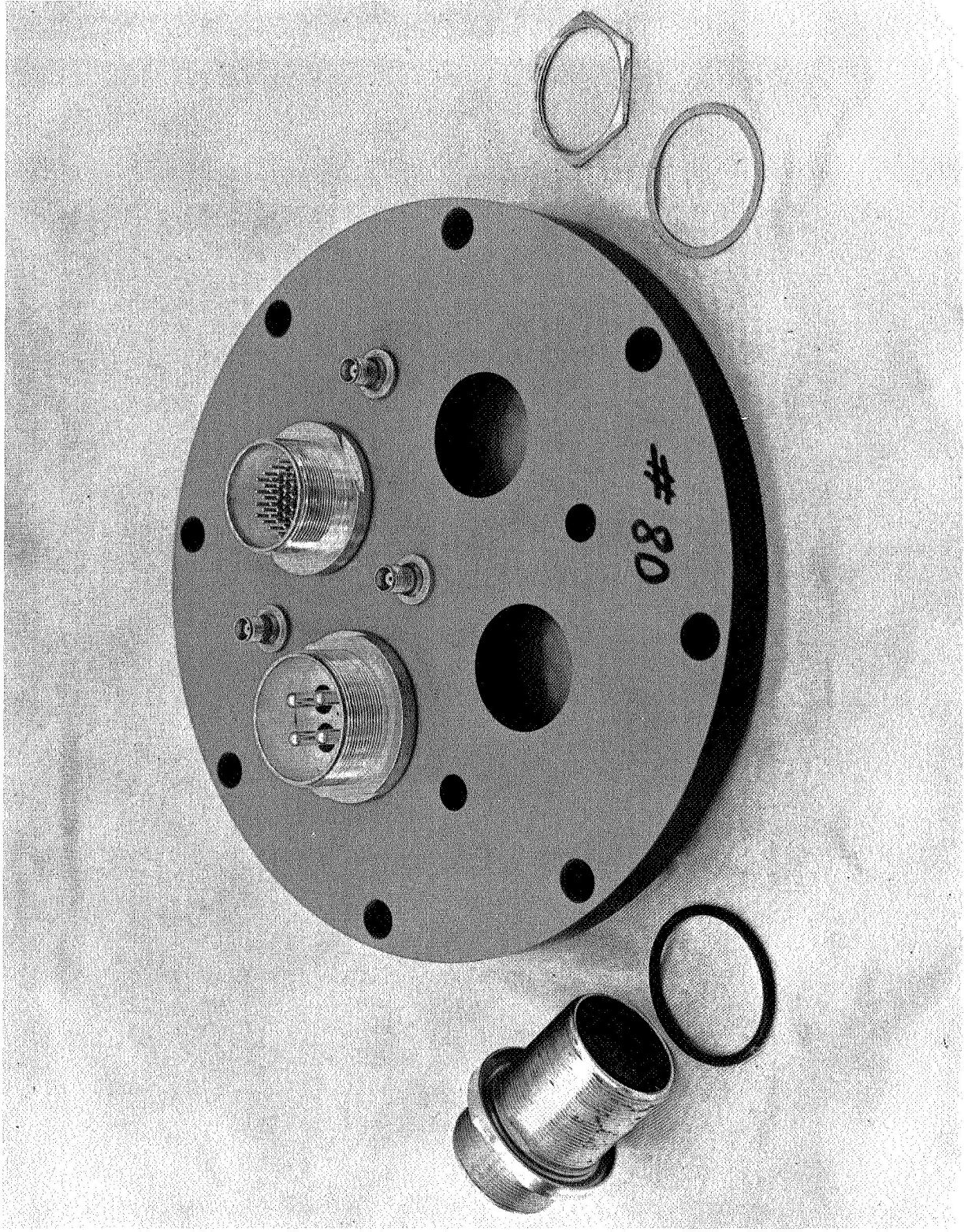


Figure 11. Phenolic Penetration Plate Assembly

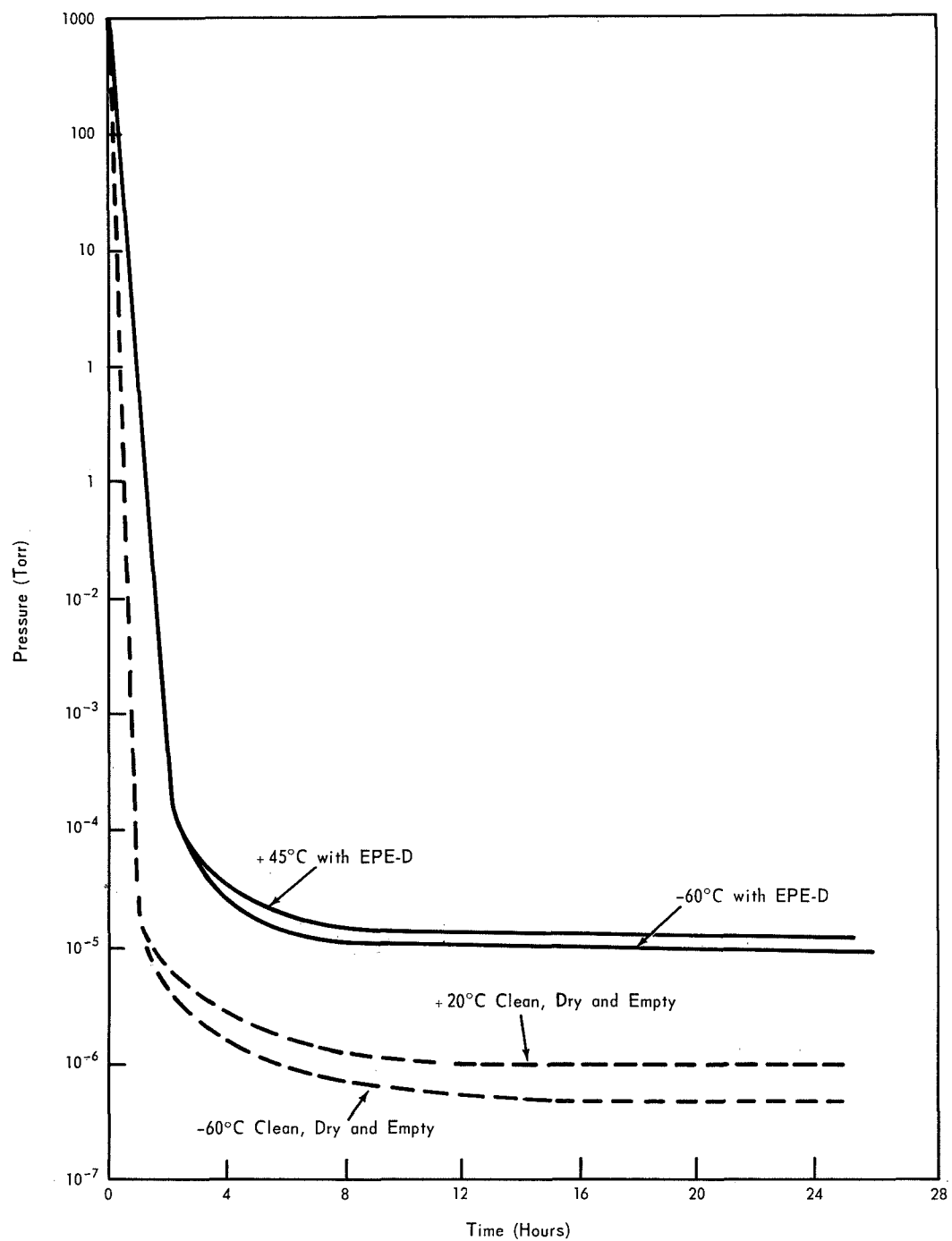


Figure 12. 8 X 8 Chamber Performance

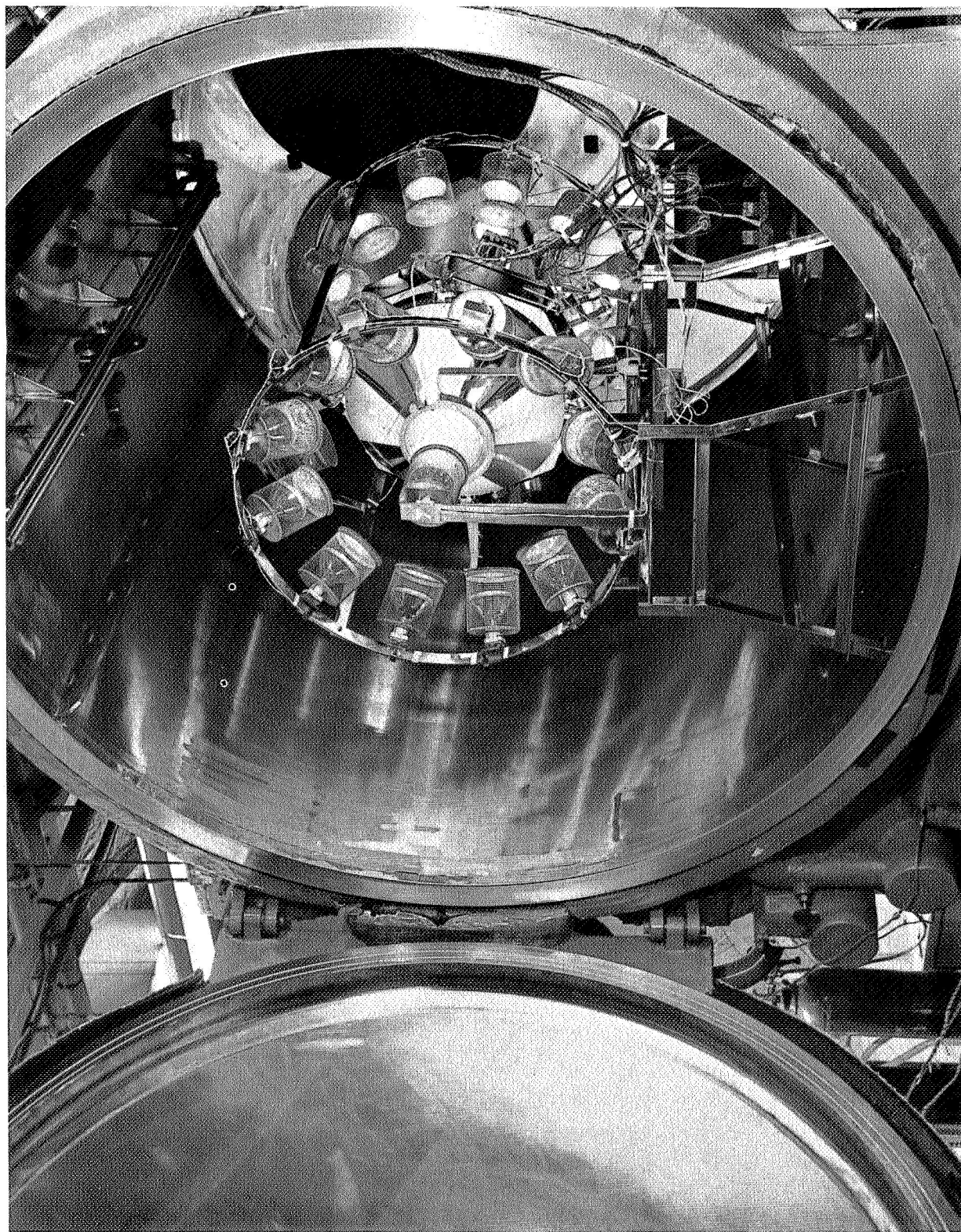


Figure 13. 8 X 8 Thermal Gradient Test Set-up

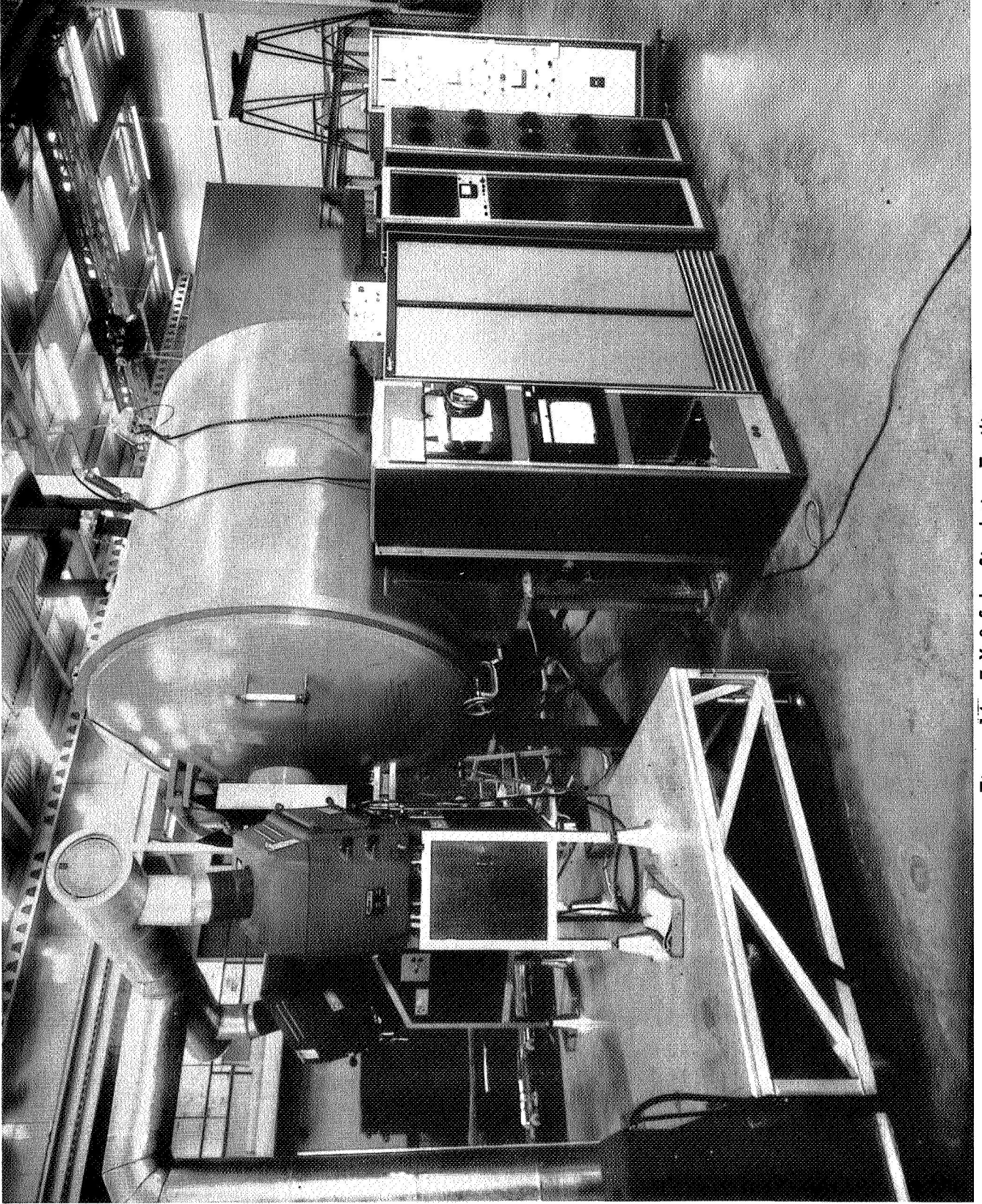


Figure 14. 7 X 8 Solar Simulation Facility

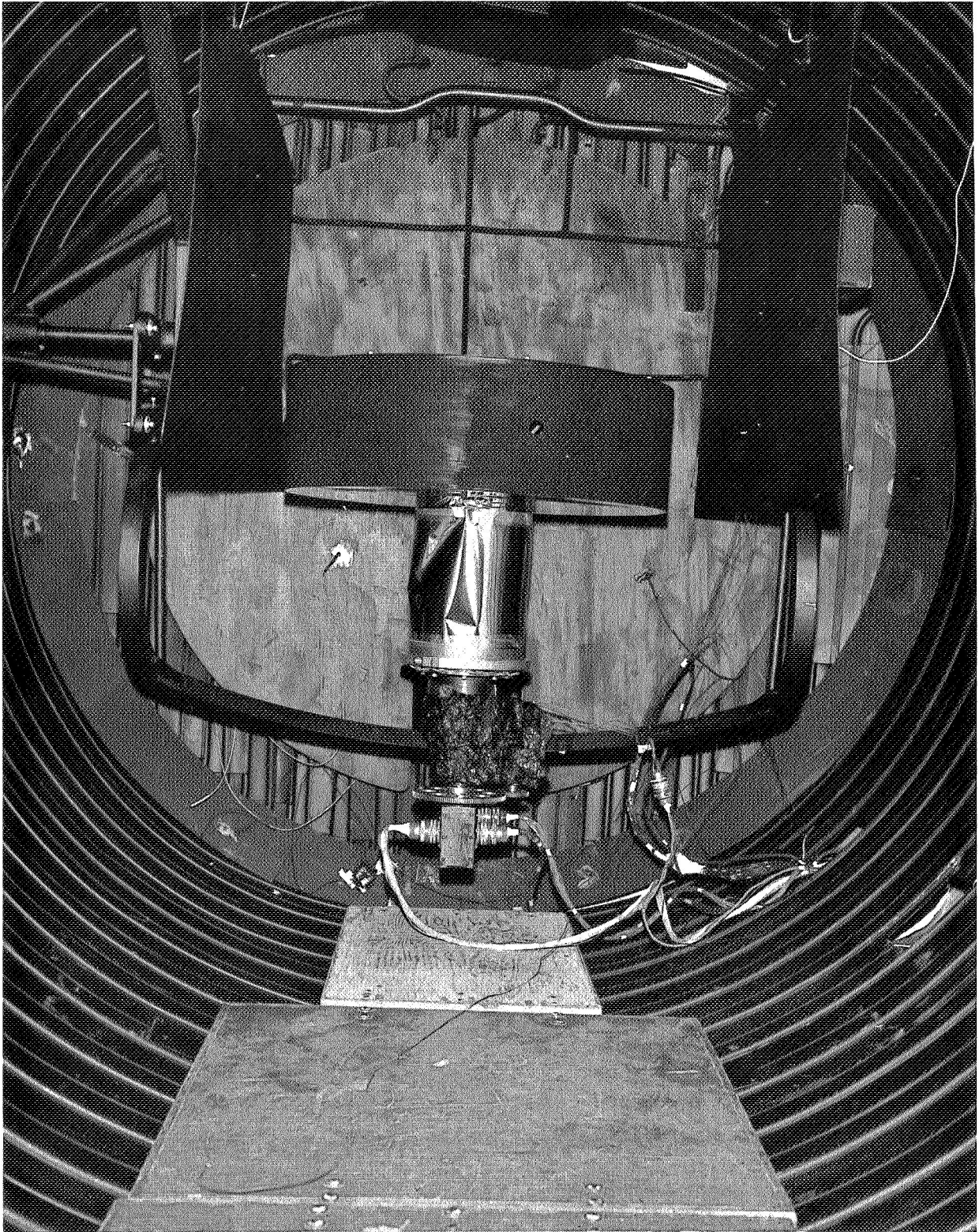


Figure 15. 7 X 8 2-Axis Spacecraft Positioner

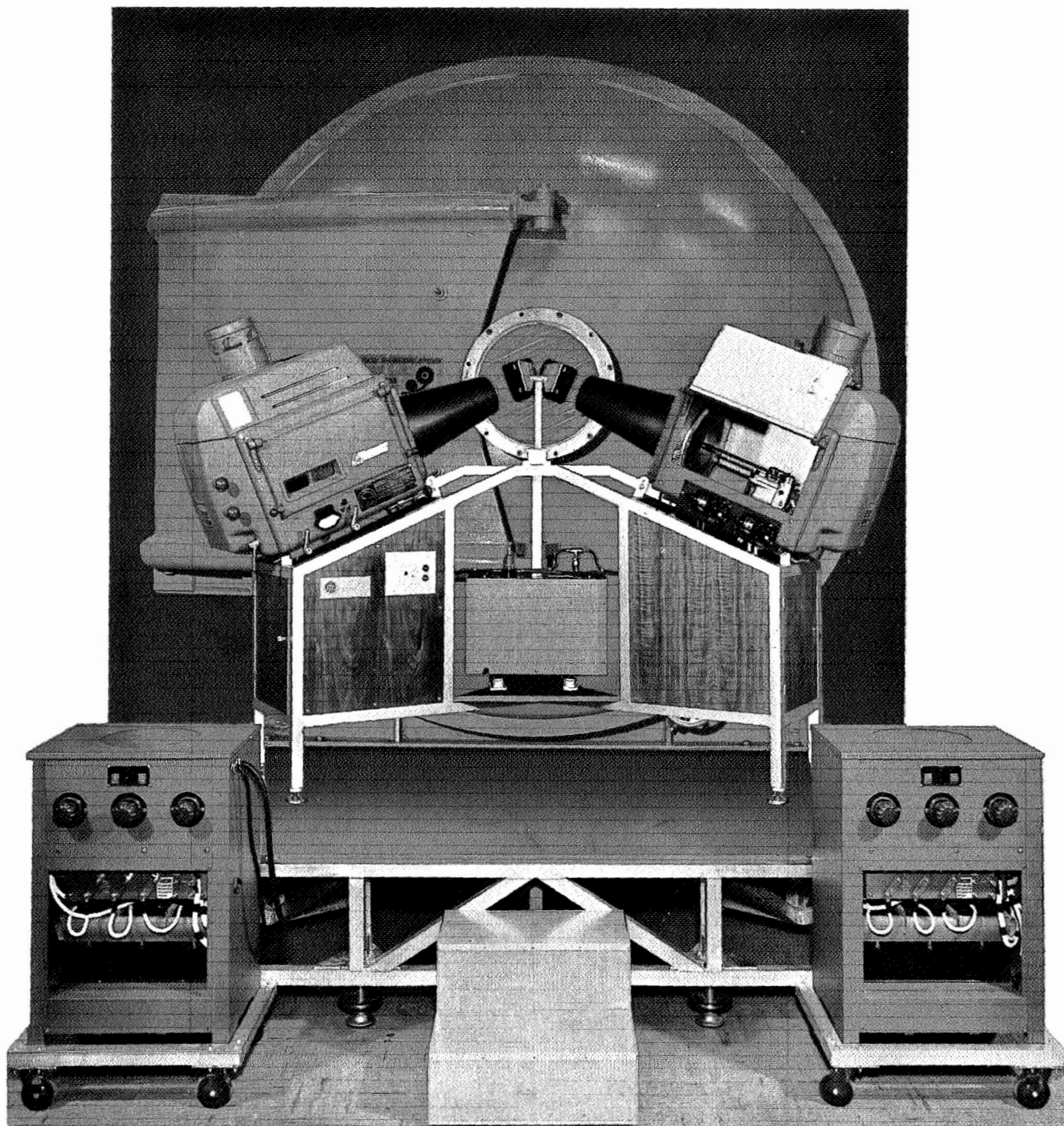


Figure 16. 7 X 8 Solar Simulation Facility



Figure 17. Carbon Arc Lamp House

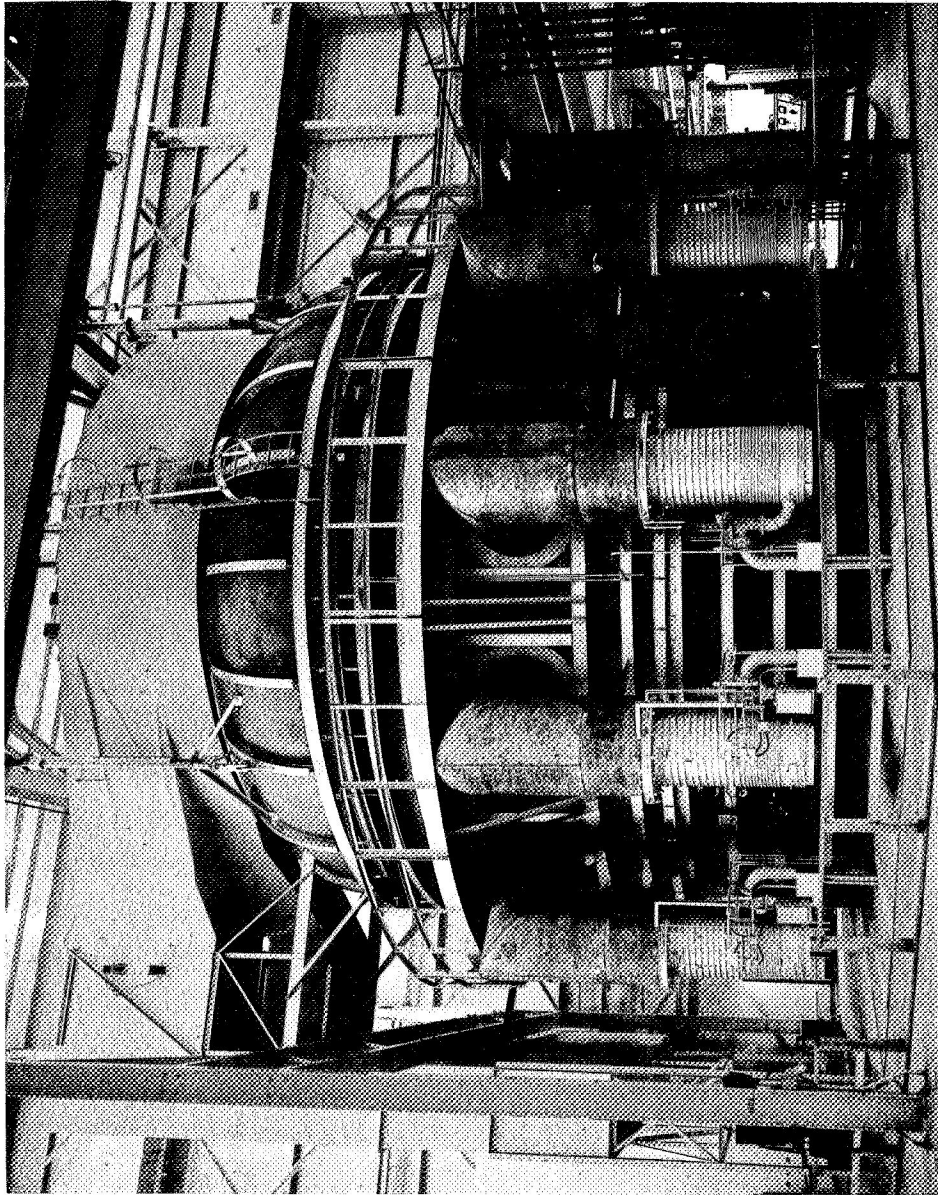


Figure 18. GSFC 30 X 30 SES

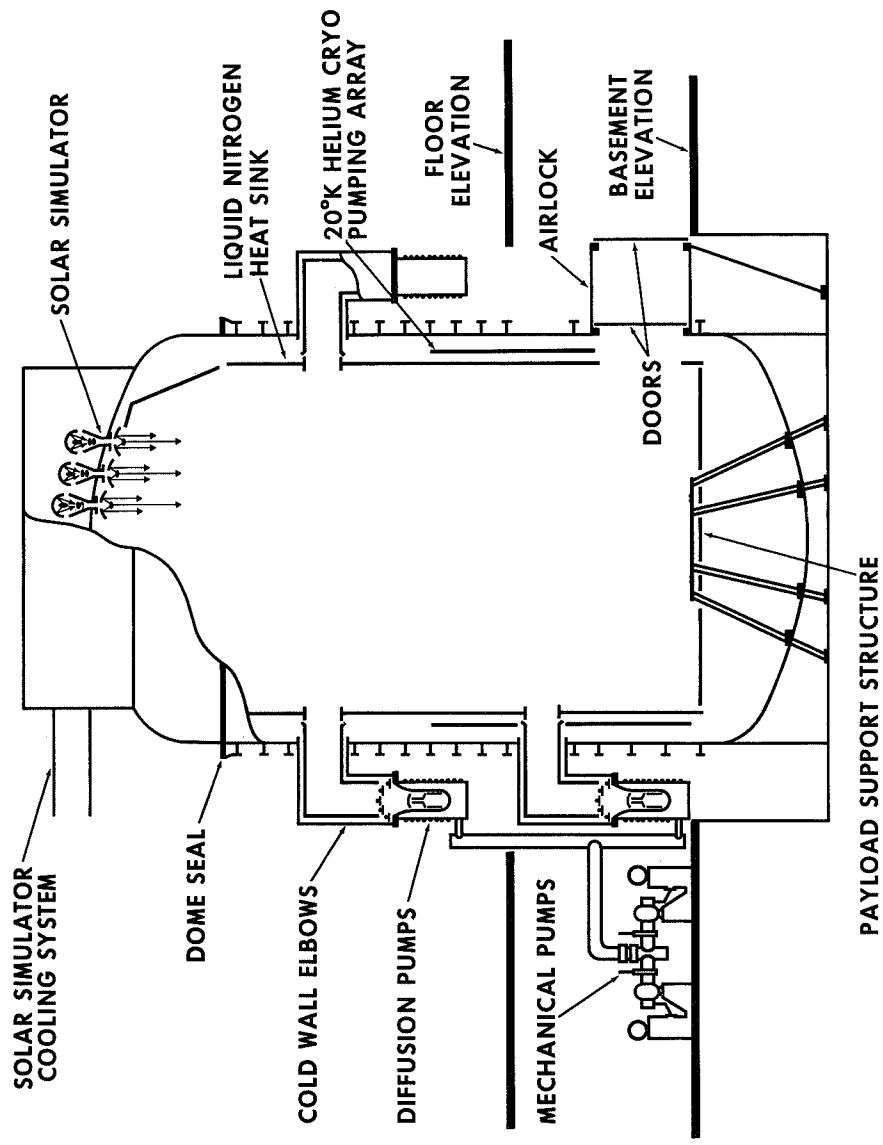


Figure 19. SES Cross Section

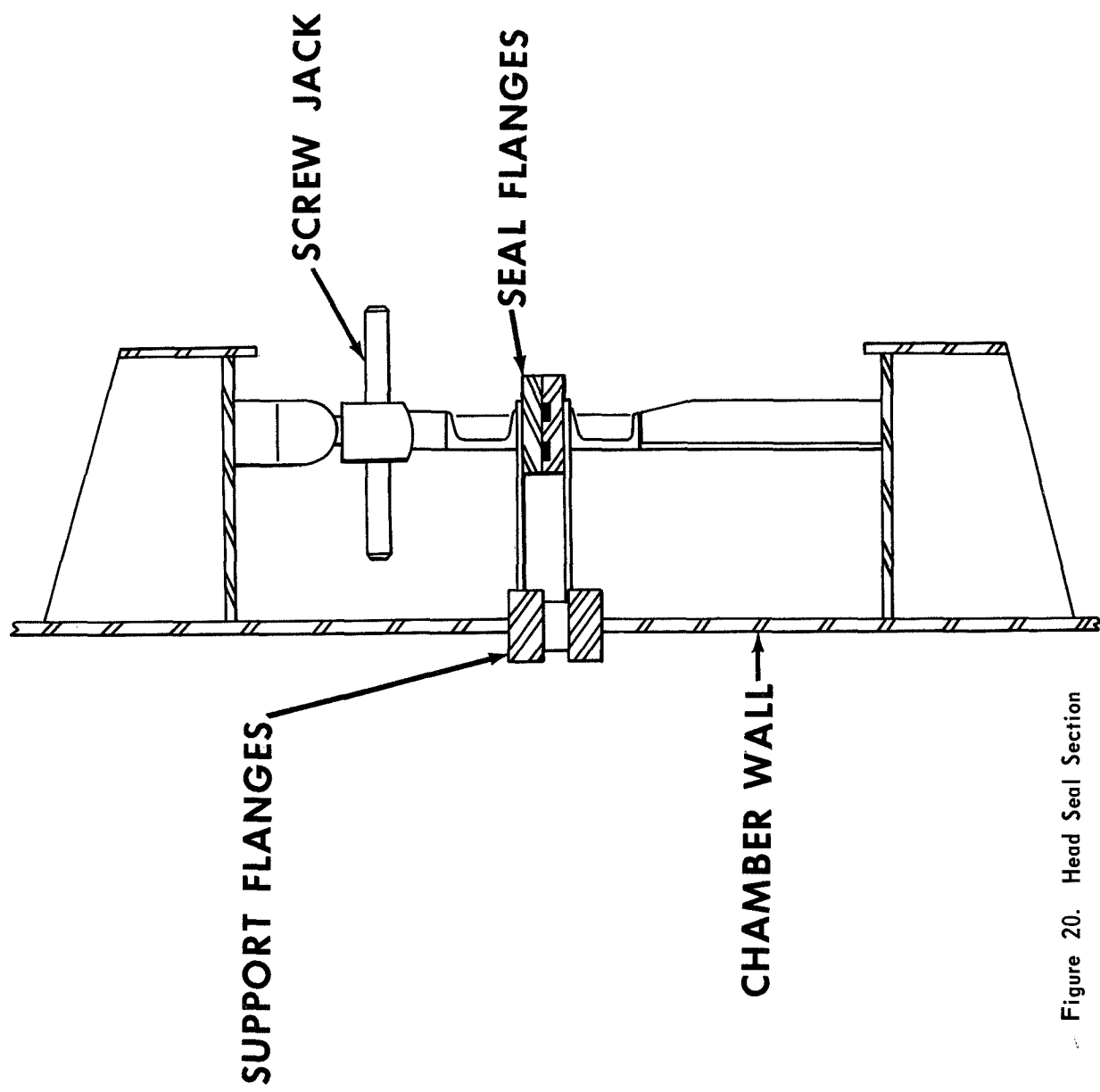
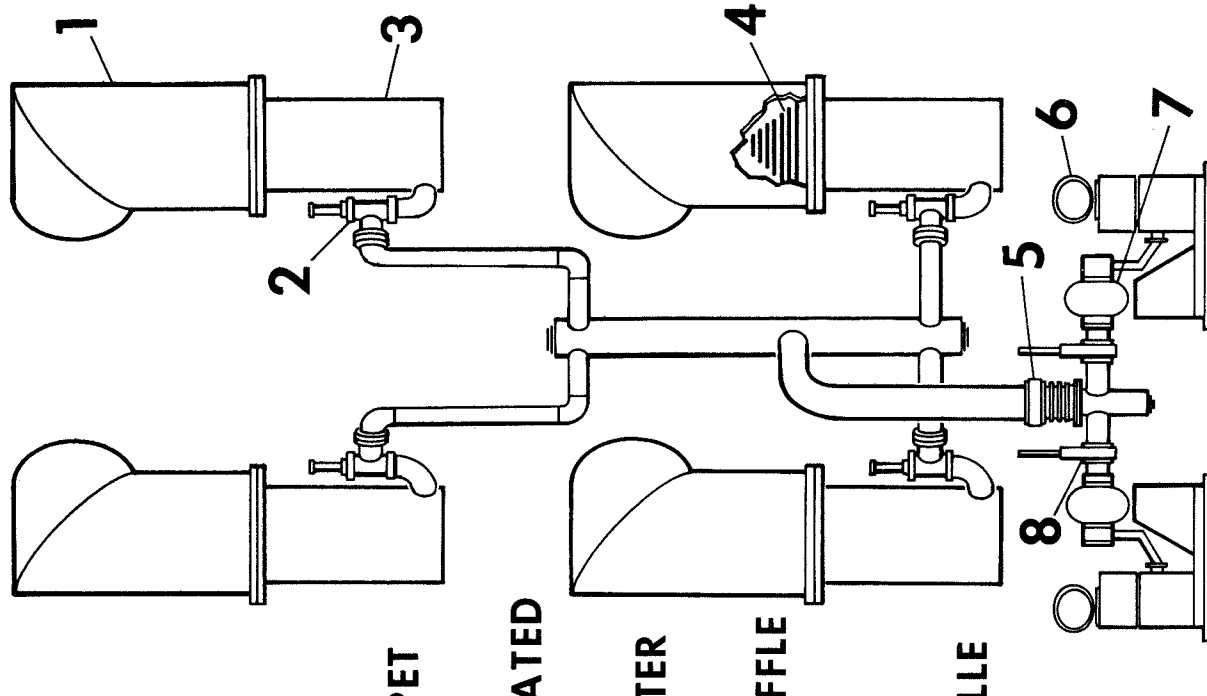


Figure 20. Head Seal Section



1. CRYOVAC LN₂ COOLED ELBOW
2. 6" STOKES AIR OPERATED POPPET VALVE
3. MODEL PMC 50,000 CONSOLIDATED DIFFUSION PUMP
4. STOKES CONCENTRIC DISC. WATER COOLED BAFFLE
5. 10" STOKES WATER COOLED BAFFLE
6. MODEL 412H STOKES VACUUM PUMP
7. MODEL 615 ROOTS CONNERSVILLE BLOWER
8. 8" TEMESCAL AIR OPERATED GATE VALVE

Figure 21. Vacuum Pumping System Schematic

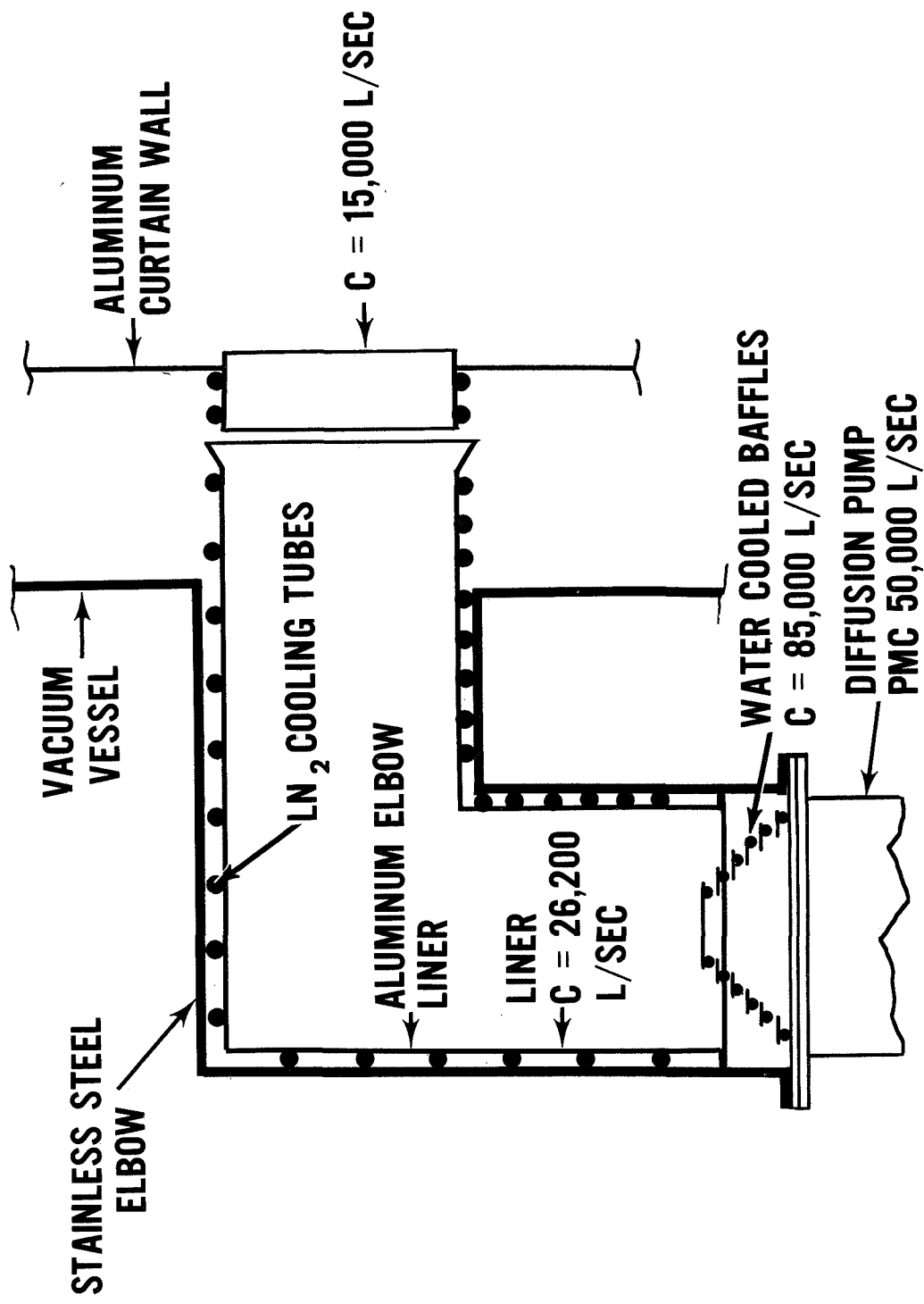


Figure 22. Cryogenic Elbow

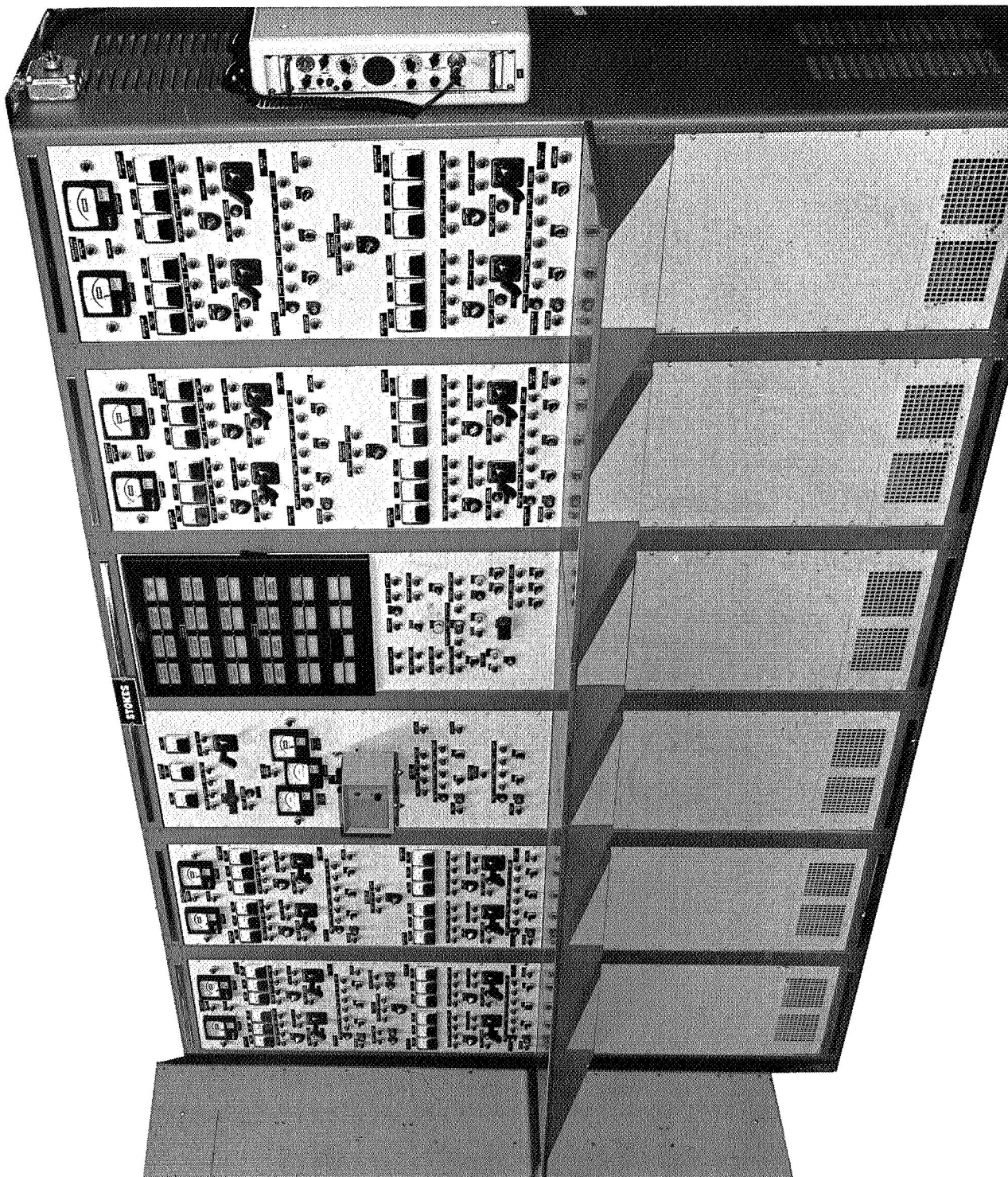


Figure 23. SES Vacuum Control Panel

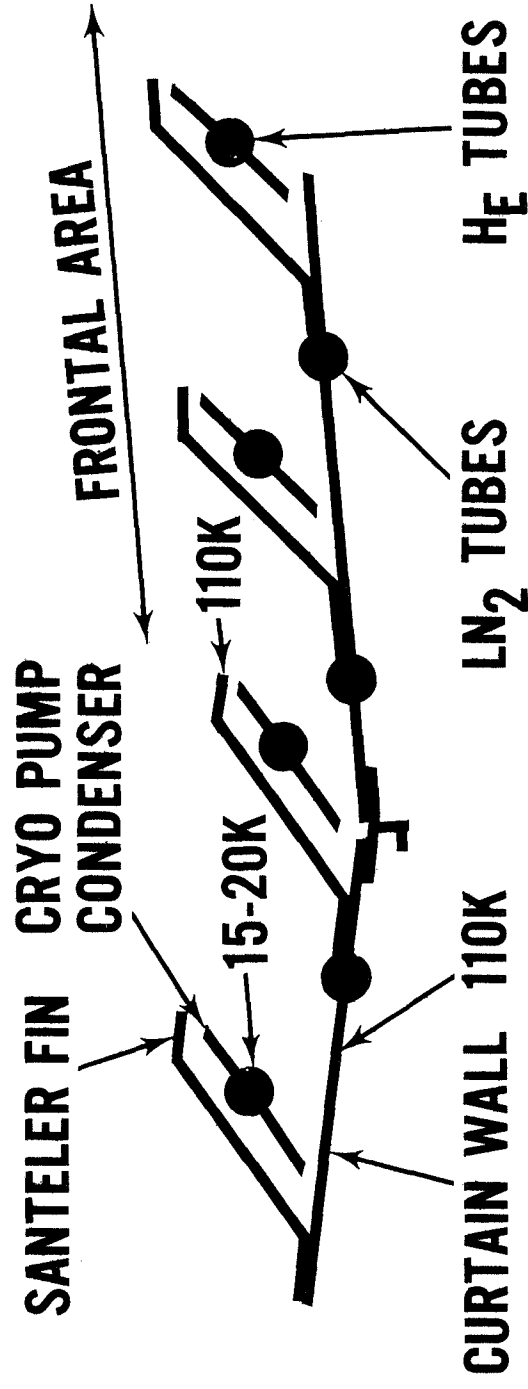


Figure 24. Curtain Wall Showing Santeler Array

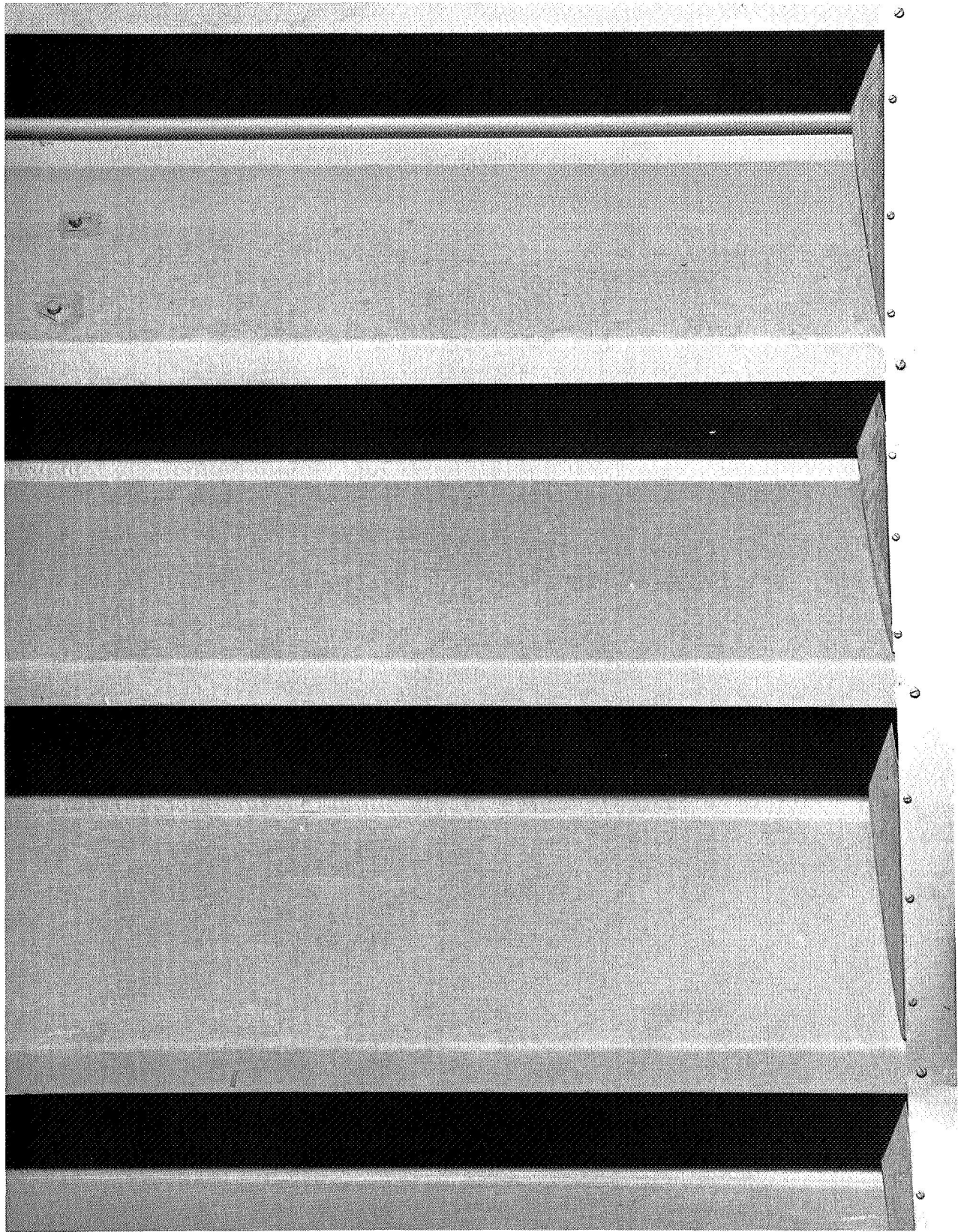


Figure 25. SES Thermal Shroud Face View

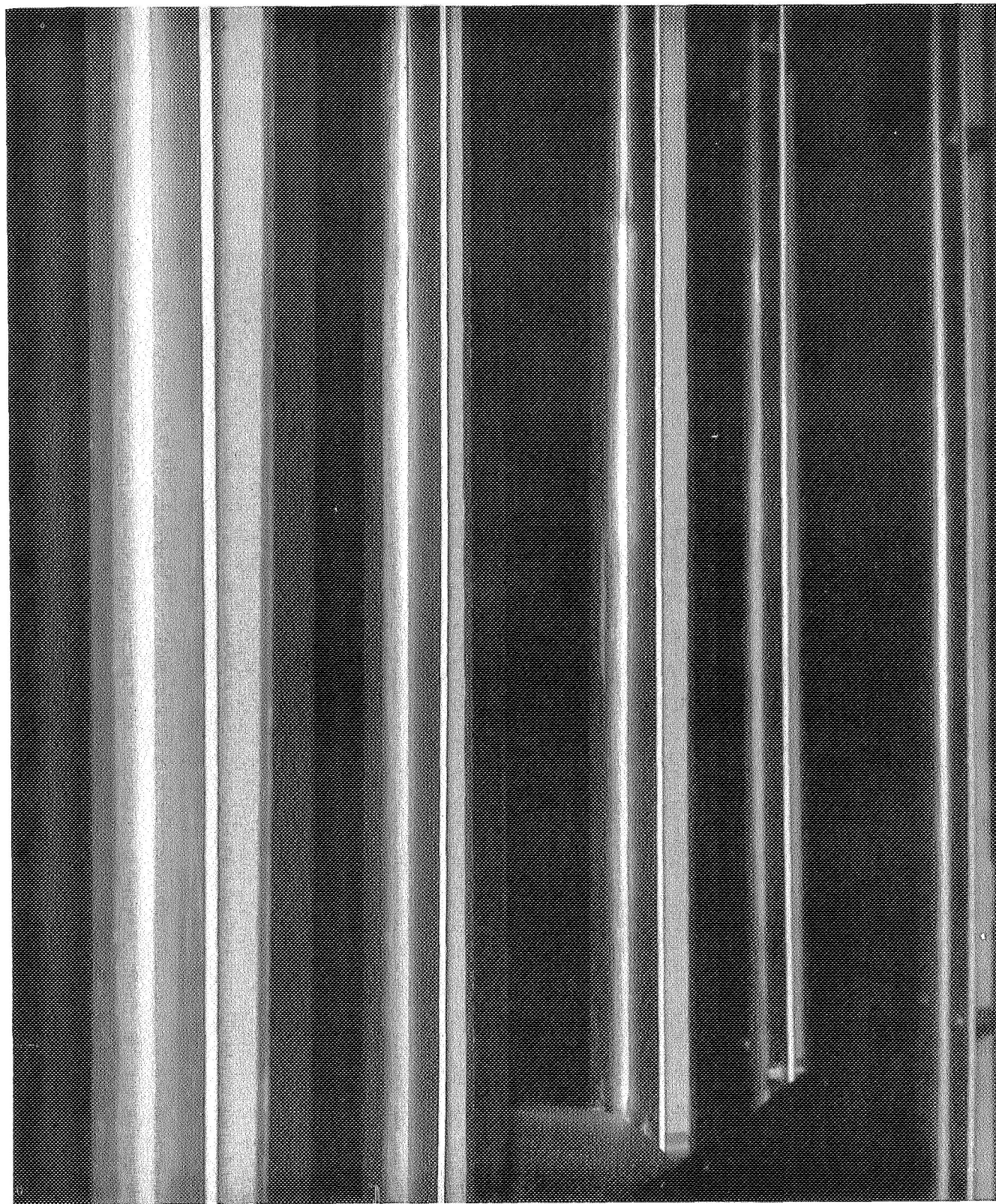


Figure 26. SES Dense Gas He Shroud behind Thermal Shroud

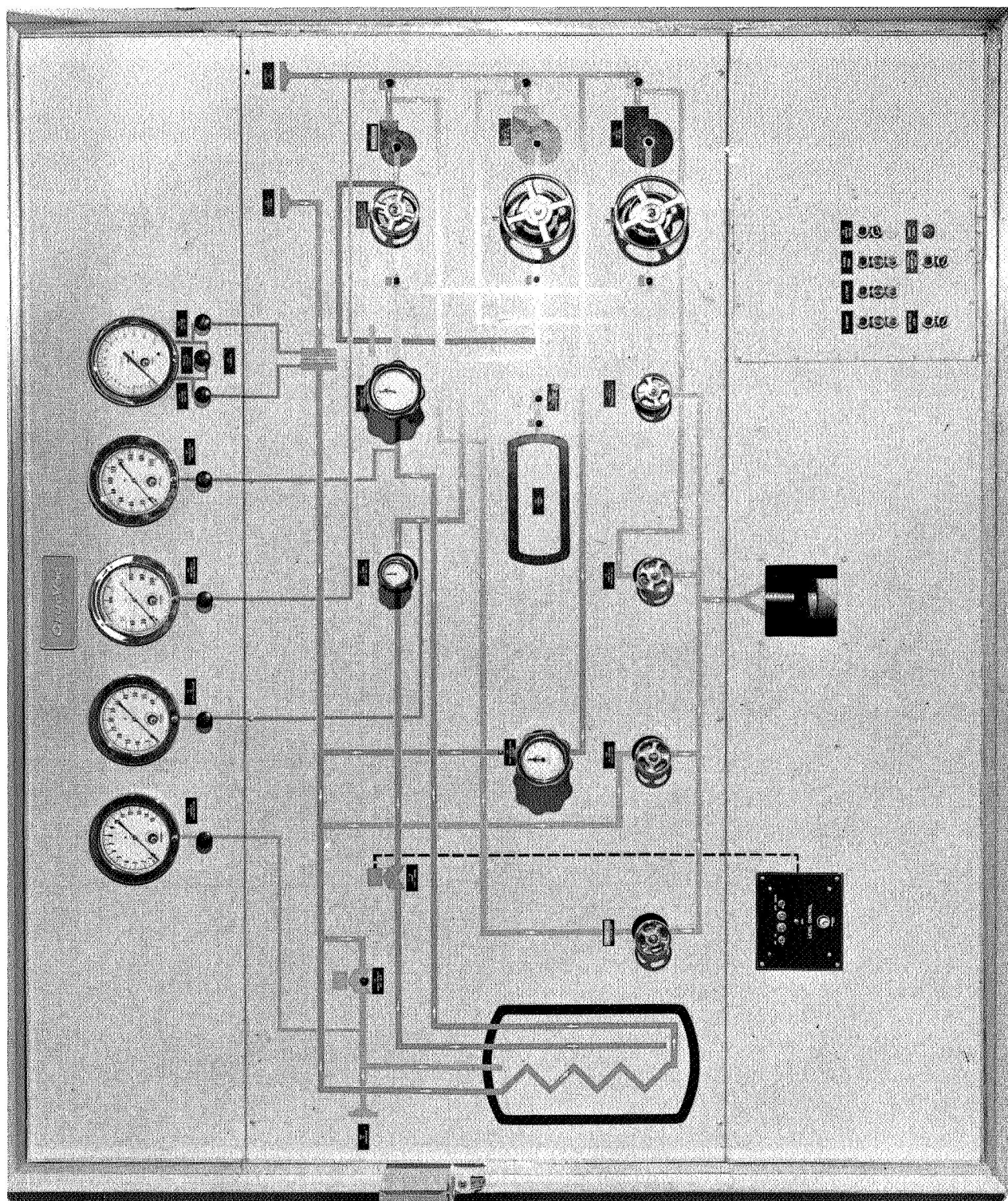


Figure 27. SES Liquid Nitrogen Supply Control Panel

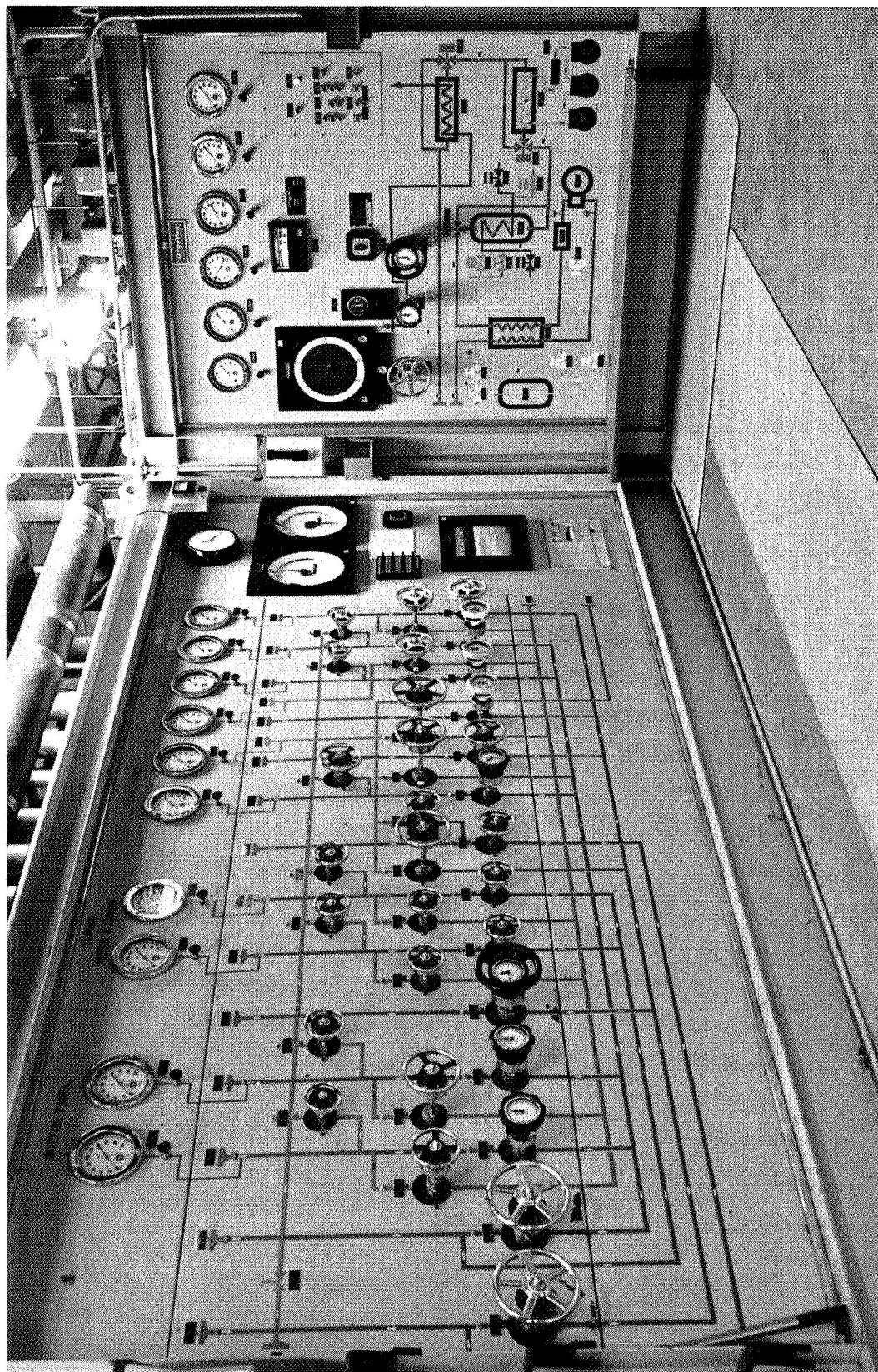


Figure 28. SES Liquid Nitrogen and Gaseous Nitrogen Control Panel

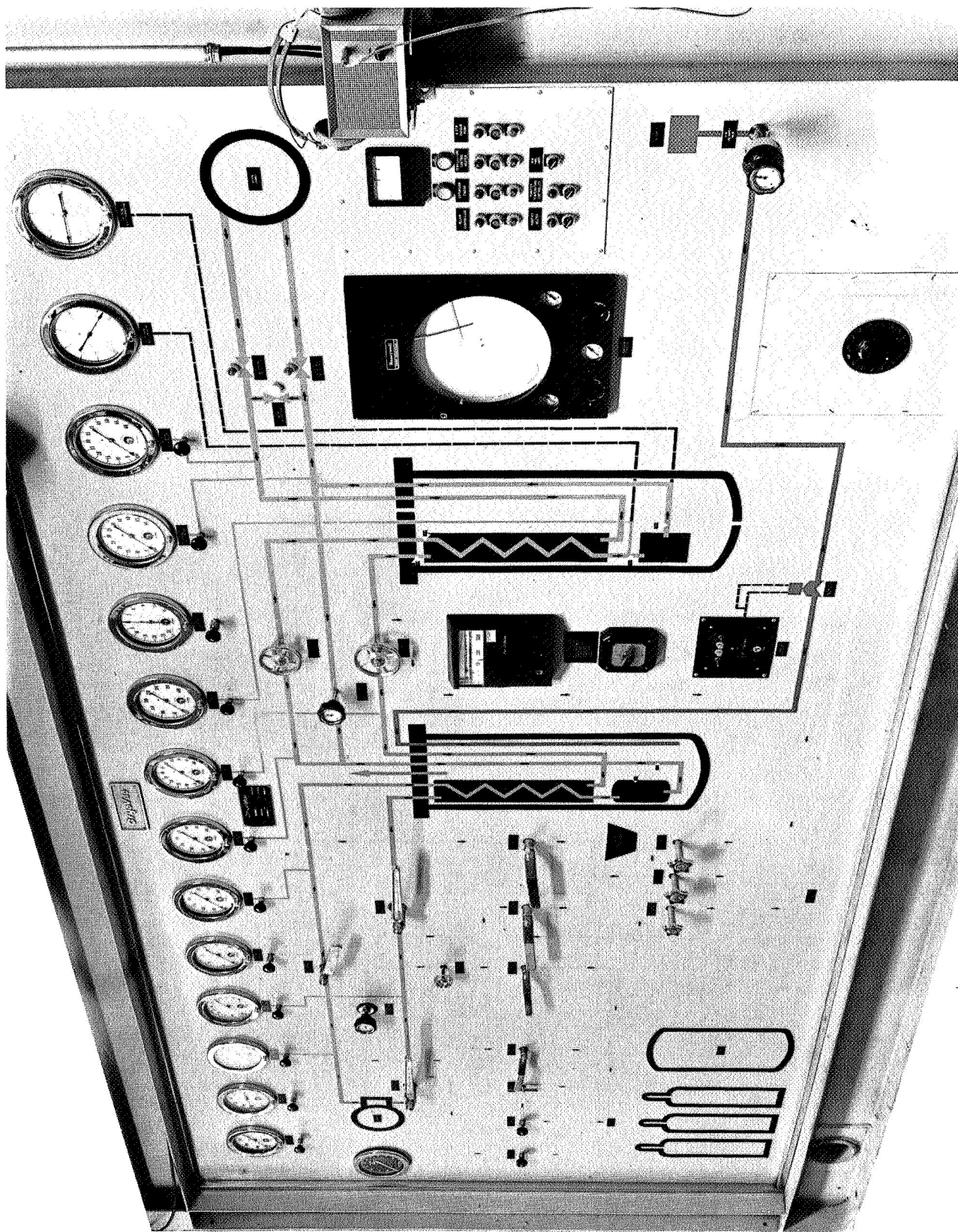


Figure 29. SES Helium Refrigerator Control Panel

SEPT. 63
49,000 ft³ VESSEL

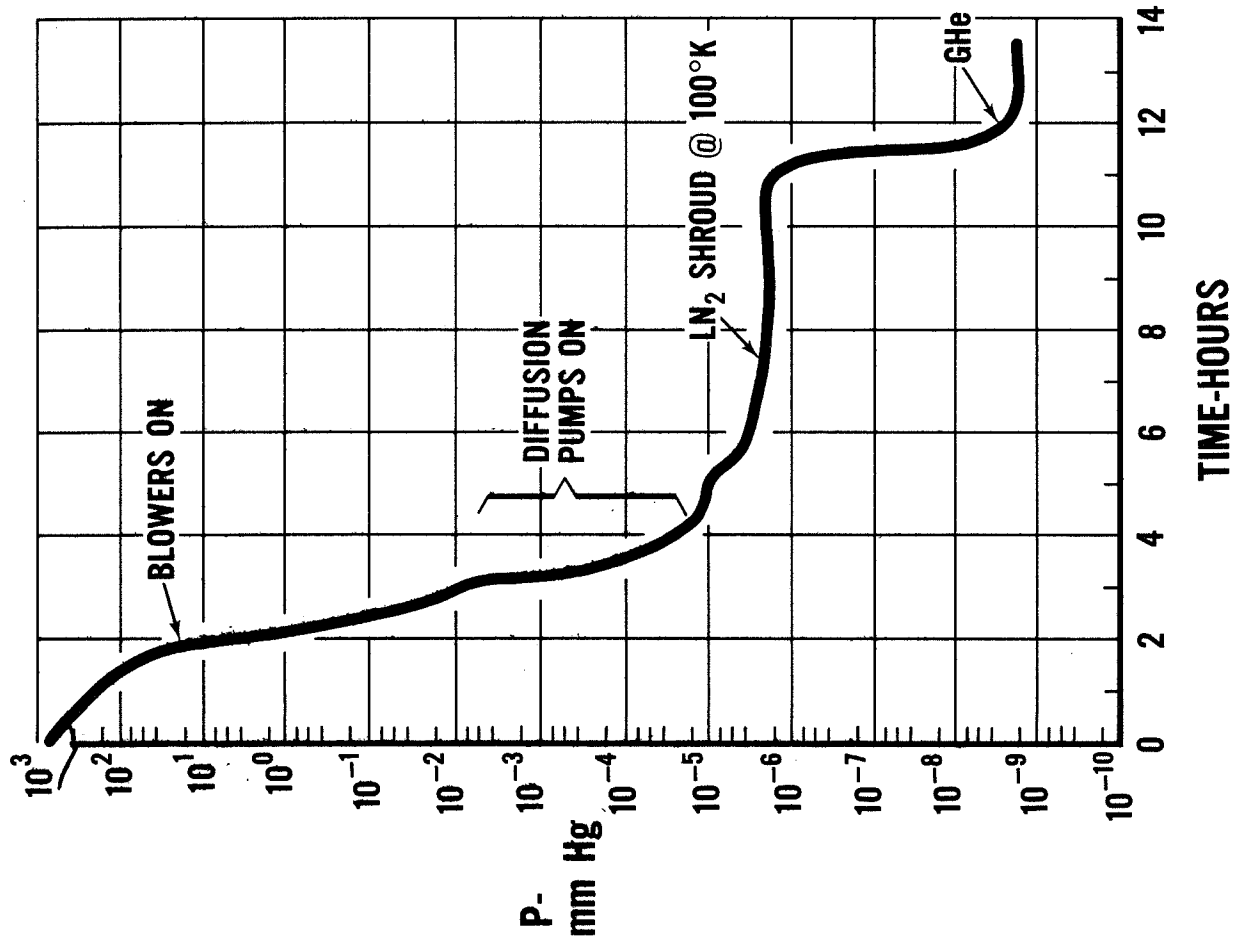


Figure 30. SES Pumpdown Curve

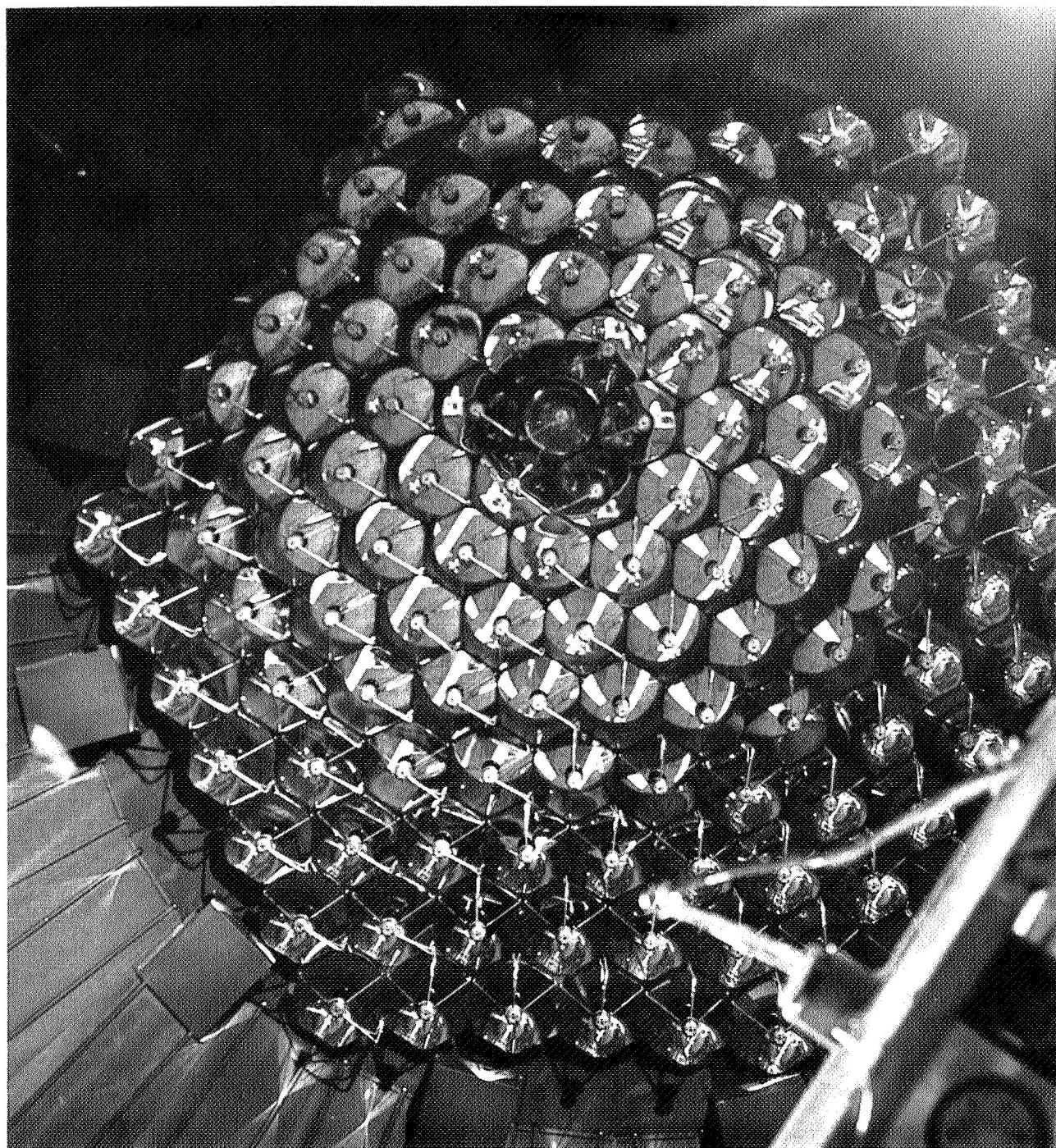


Figure 31. SES Modular Sun at 40' Distance

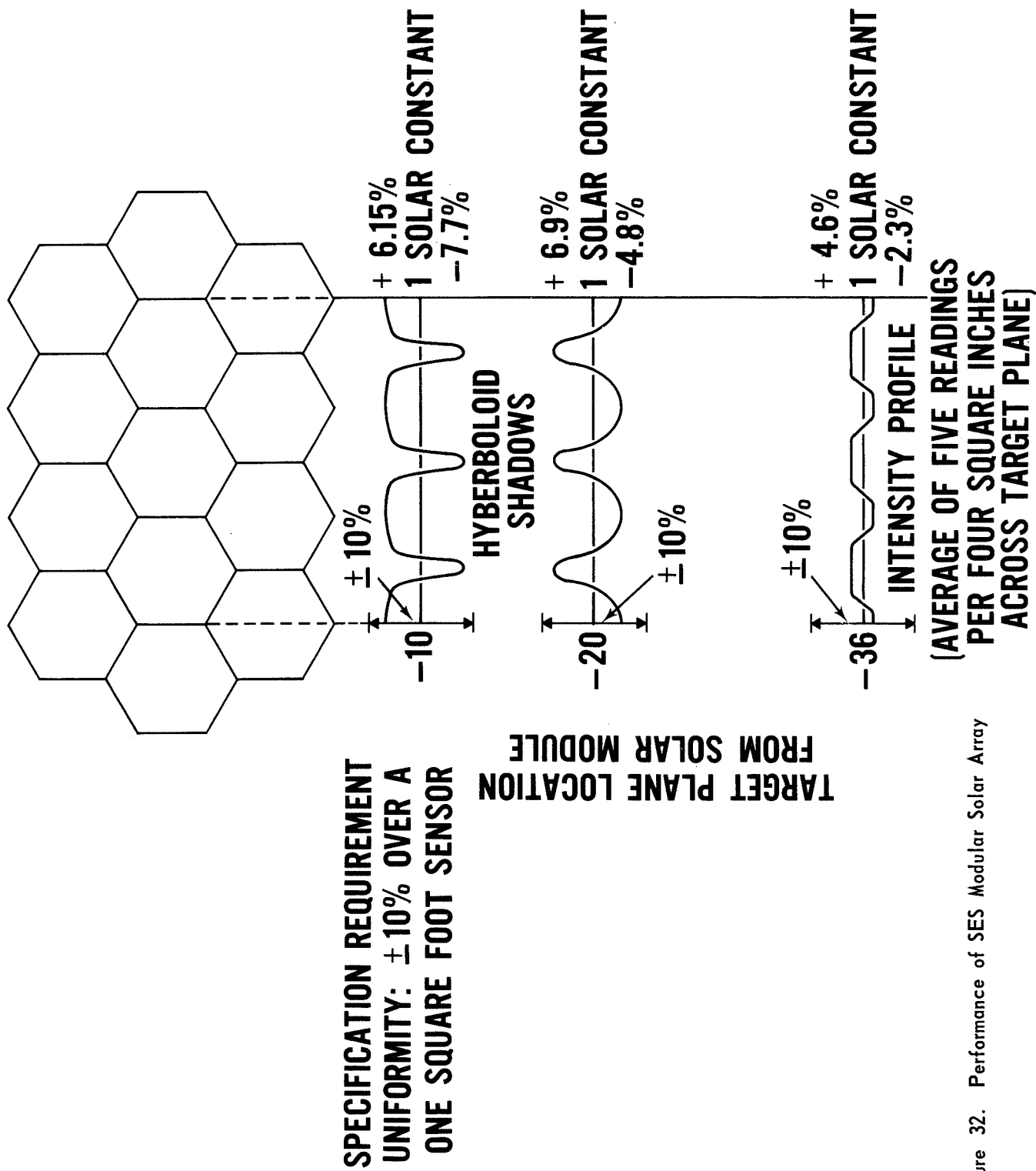


Figure 32. Performance of SES Modular Solar Array

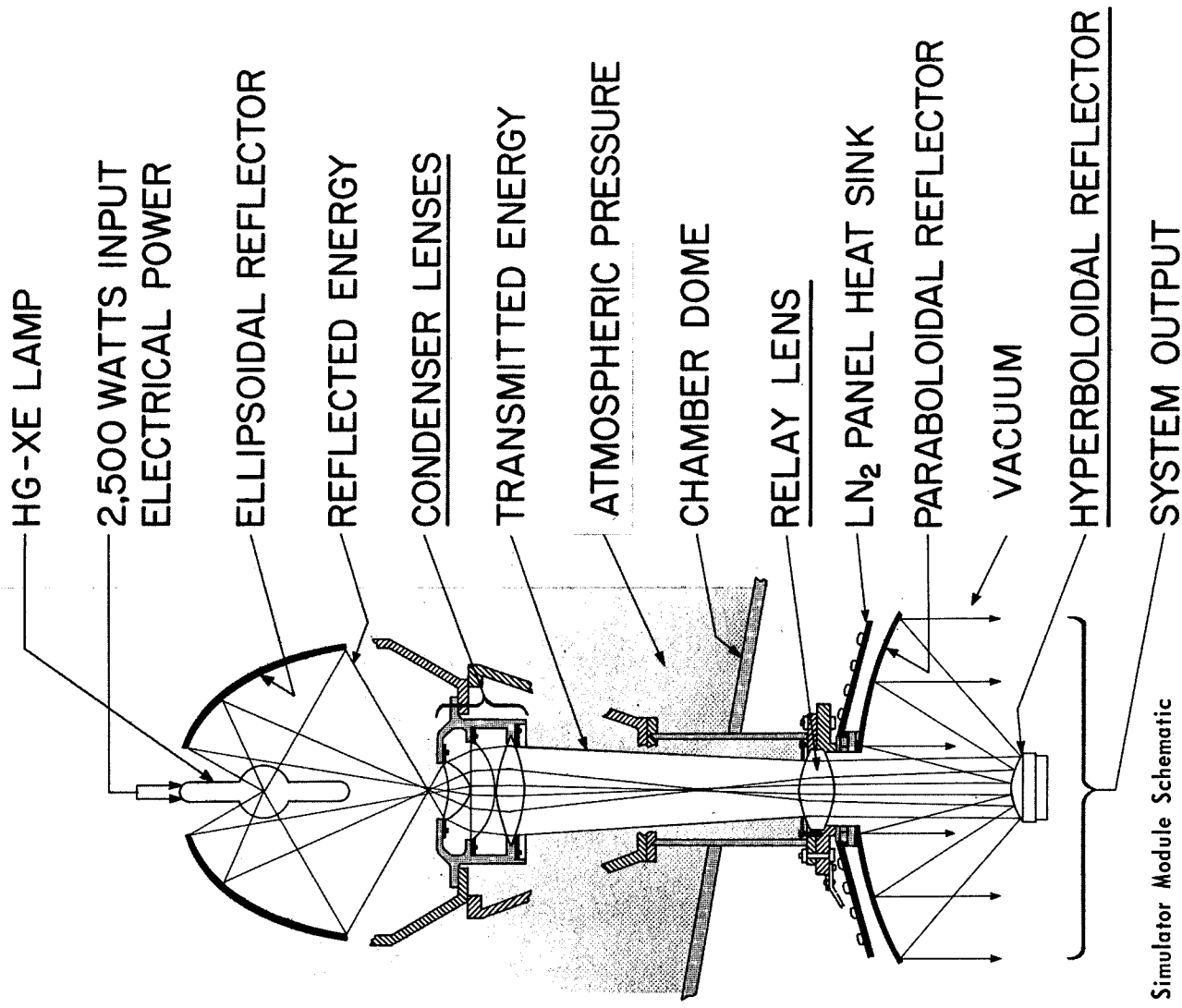


Figure 33. Solar Simulator Module Schematic

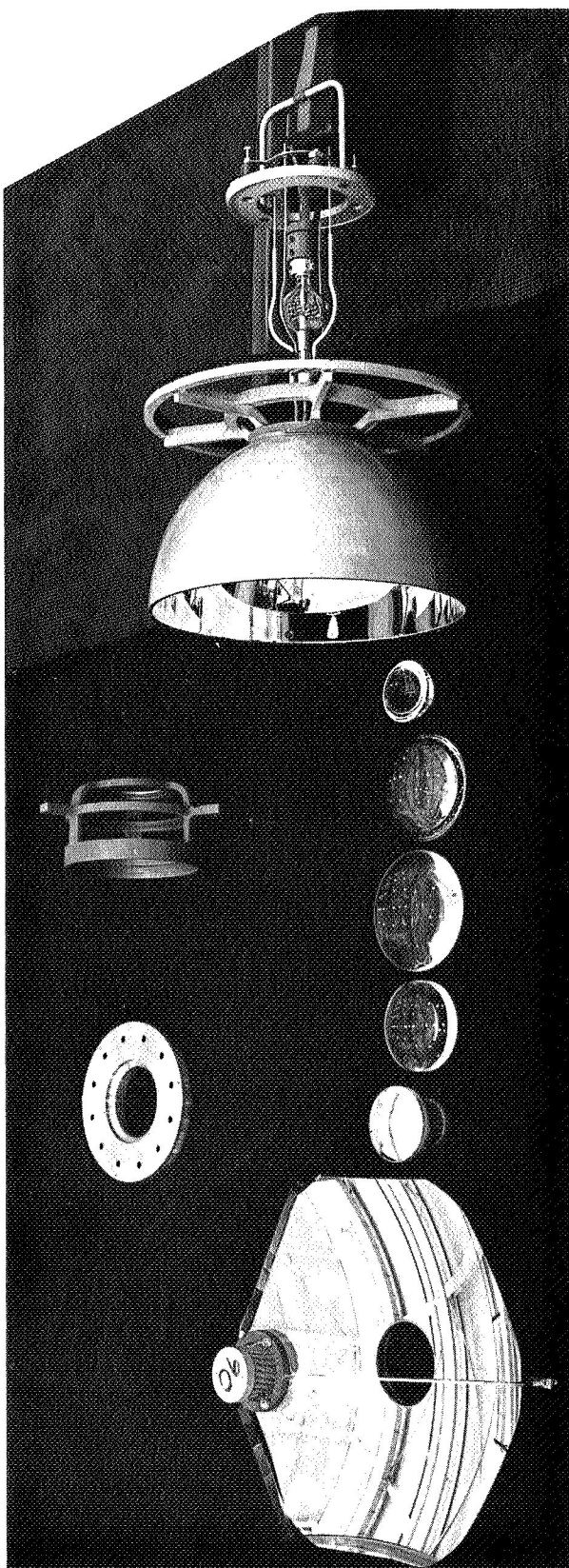


Figure 34. SES Solar Module Elements

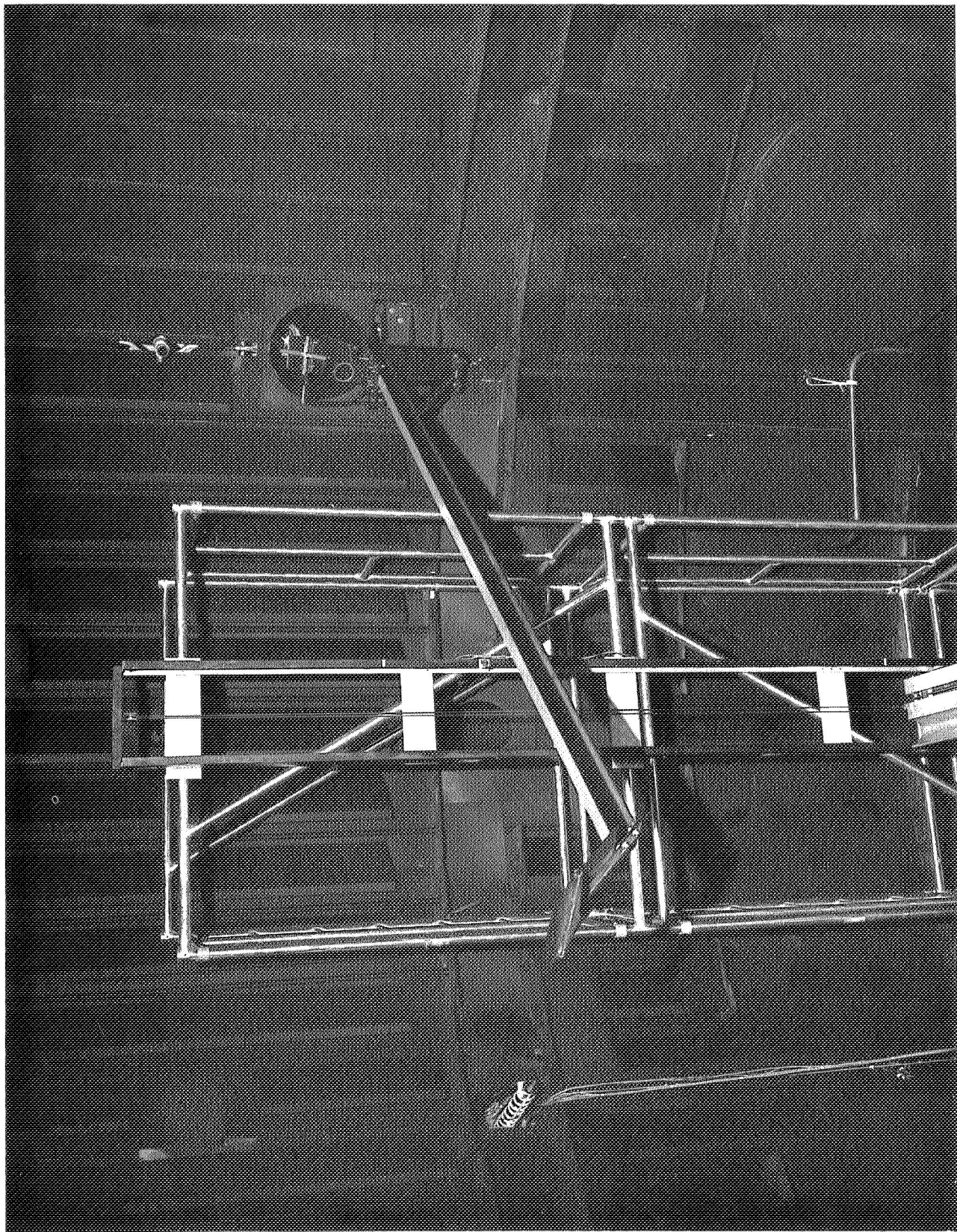


Figure 35. SES 20' Spectrum Monitor Boom

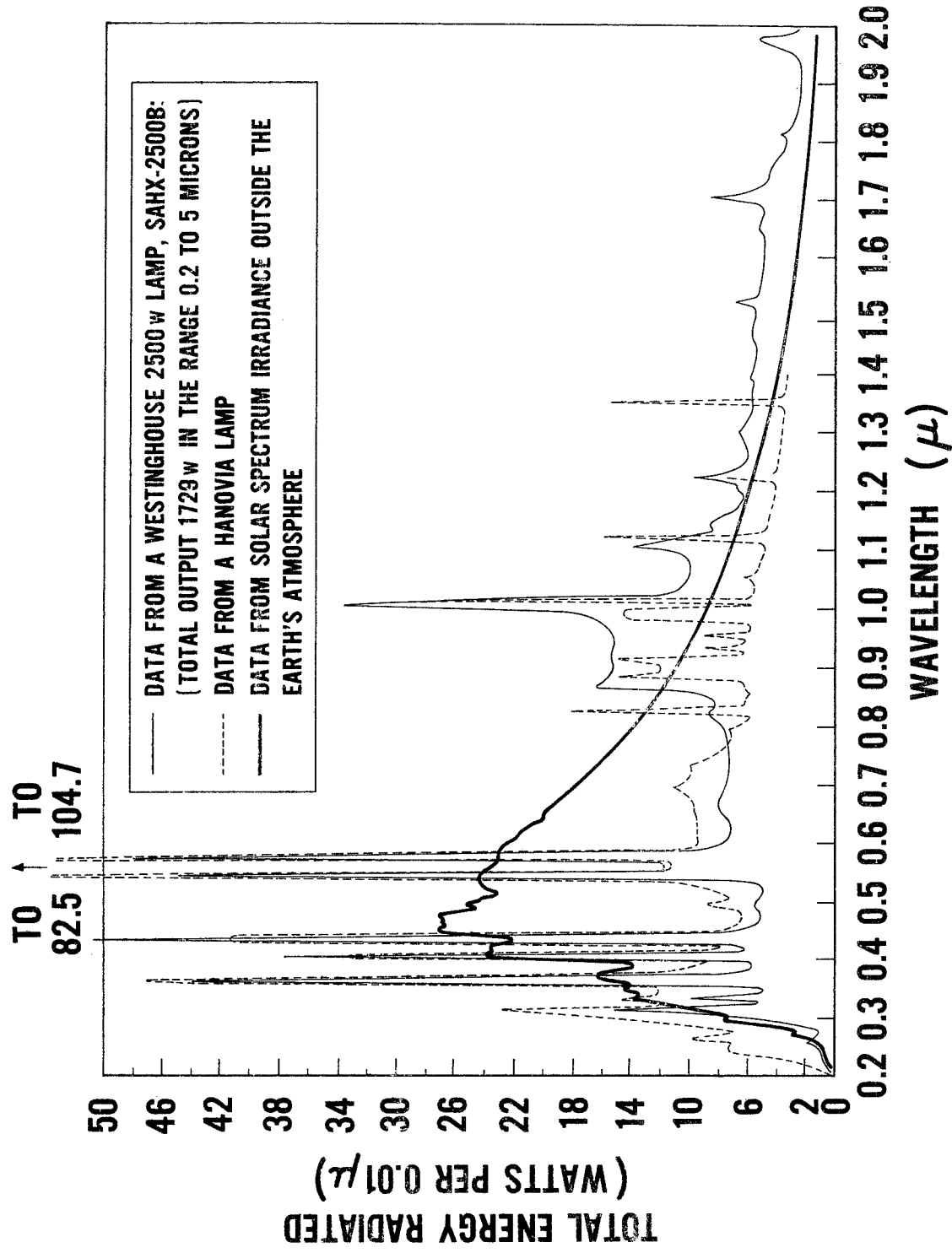


Figure 36. Spectral-Energy Distribution of Typical Hg-Xe Lamps Vs Solar Radiation



Figure 37. SES Master Control Console

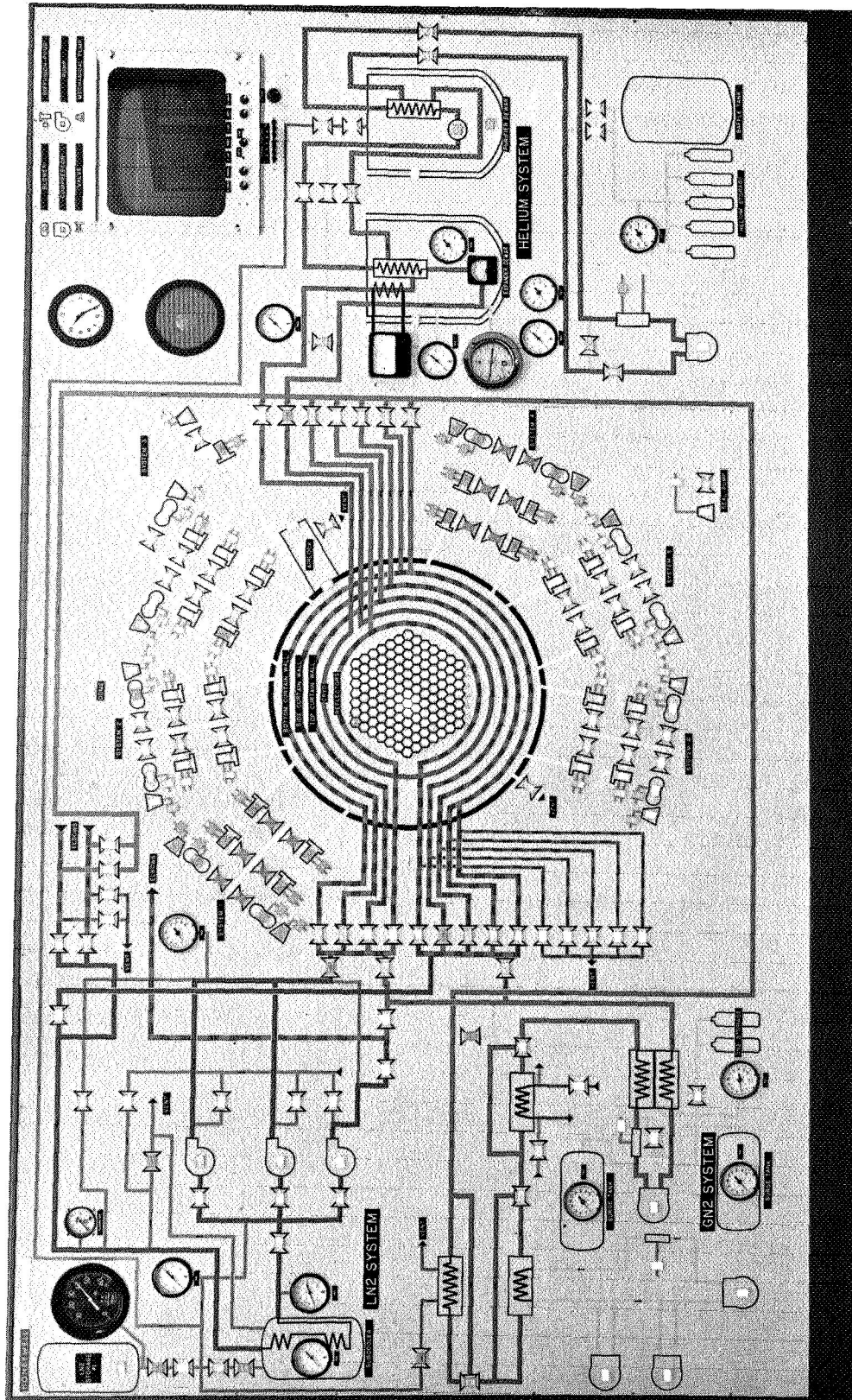


Figure 38. SES Graphic Mimic Master Display

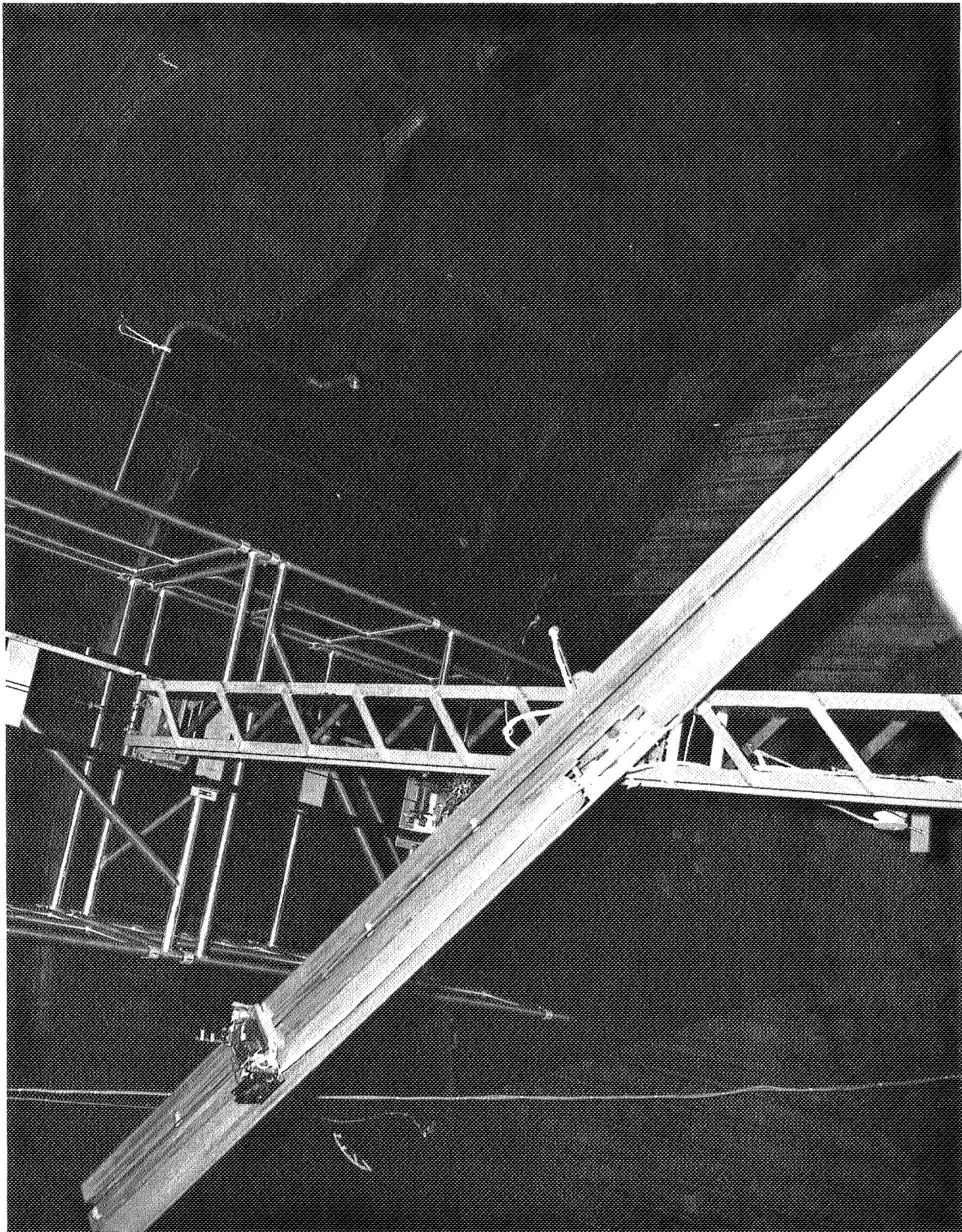


Figure 39. SES R-Ø-Z Intensity Scanner

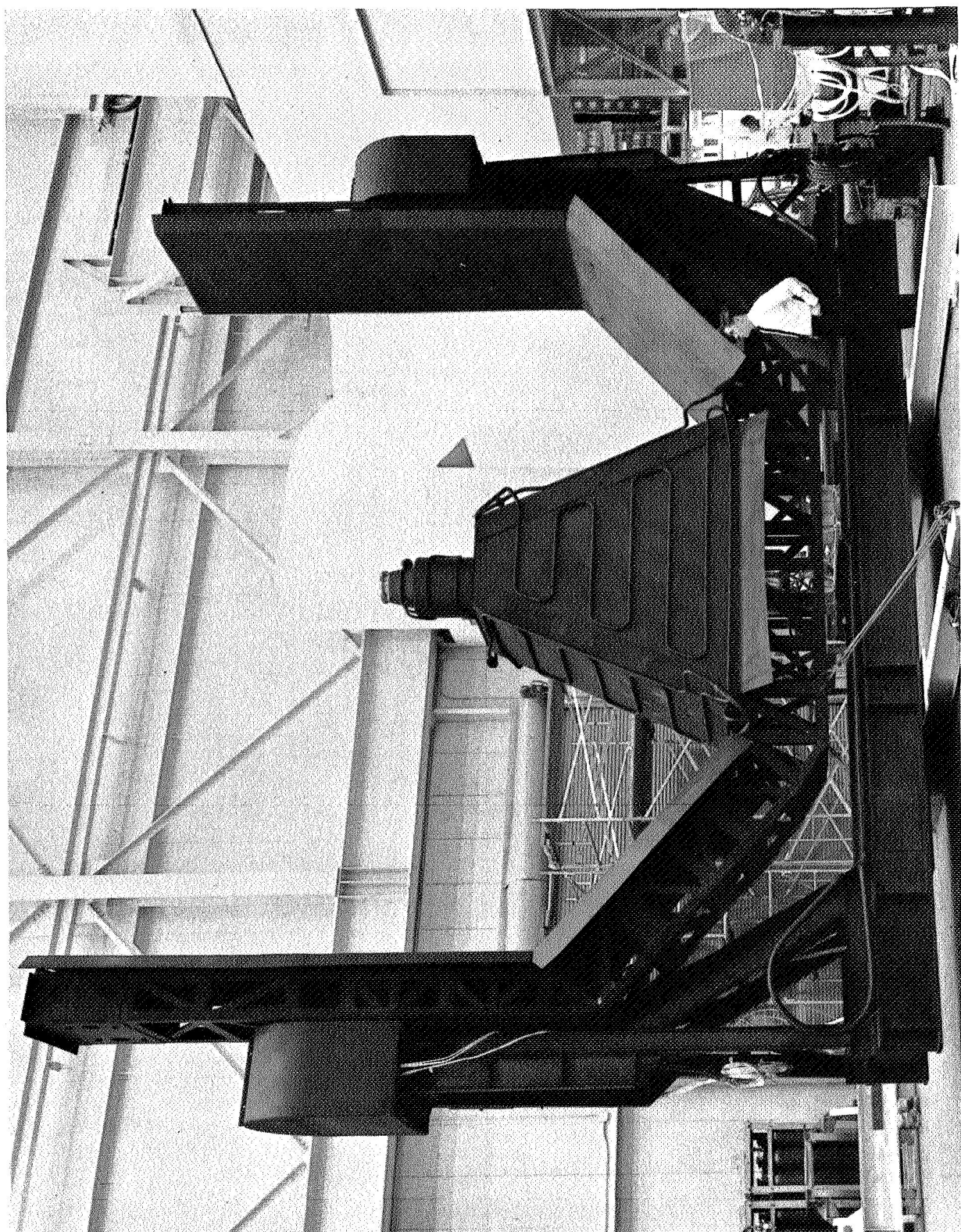


Figure 40. SES 2-Axis Spacecraft Positioner